

# The distribution of gas in the Local Group from constrained cosmological simulations: the case for Andromeda and the Milky Way galaxies

Sebastián E. Nuza<sup>1\*</sup>, Florencia Parisi<sup>1,2</sup>, Cecilia Scannapieco<sup>1</sup>, Philipp Richter<sup>1,3</sup>, Stefan Gottlöber<sup>1</sup> and Matthias Steinmetz<sup>1</sup>

<sup>1</sup> *Leibniz-Institut für Astrophysik Potsdam (AIP), An der Sternwarte 16, D-14482, Potsdam, Germany*

<sup>2</sup> *Consejo Nacional de Investigaciones Científicas y Técnicas (CONICET), Argentina*

<sup>3</sup> *Institut für Physik und Astronomie, Universität Potsdam, Haus 28, Karl-Liebknecht-Str. 24/25, 14476 Golm (Potsdam), Germany*

1 April 2014

## ABSTRACT

We study the gas distribution in the Milky Way and Andromeda using a constrained cosmological simulation of the Local Group (LG) within the context of the CLUES (Constrained Local UniversE Simulations) project. We analyse the properties of gas in the simulated galaxies at  $z = 0$  for three different phases: ‘cold’, ‘hot’ and H I, and compare our results with observations. The amount of material in the hot halo ( $M_{\text{hot}} \approx 4 - 5 \times 10^{10} M_{\odot}$ ), and the cold ( $M_{\text{cold}}(r \lesssim 10 \text{ kpc}) \approx 10^8 M_{\odot}$ ) and H I ( $M_{\text{HI}}(r \lesssim 50 \text{ kpc}) \approx 3 - 4 \times 10^8 M_{\odot}$ ) components display a reasonable agreement with observations. We also compute the accretion/ejection rates together with the H I (radial and all-sky) covering fractions. The integrated H I accretion rate within  $r = 50 \text{ kpc}$  gives  $\sim 0.2 - 0.3 M_{\odot} \text{ yr}^{-1}$ , i.e. close to that obtained from high-velocity clouds in the Milky Way. We find that the global accretion rate is dominated by hot material, although ionized gas with  $T \lesssim 10^5 \text{ K}$  can contribute significantly too. The *net* accretion rates of *all* material at the virial radii are  $6 - 8 M_{\odot} \text{ yr}^{-1}$ . At  $z = 0$ , we find a significant gas excess between the two galaxies, as compared to any other direction, resulting from the overlap of their gaseous haloes. In our simulation, the gas excess first occurs at  $z \sim 1$ , as a consequence of the kinematical evolution of the LG.

**Key words:** cosmology: large scale structure of Universe – galaxies: Local Group – galaxies: intergalactic medium – Galaxy: halo – methods: numerical

## 1 INTRODUCTION

The distribution of gas in galaxies, their haloes and their adjacent regions is a key aspect of galaxy formation and evolution and can give us important clues on the current evolutionary state of the galactic systems, as well as on their recent past history. For instance, the presence of cold, inflowing gas, may point towards an immediate future of active star formation, whereas the existence of outflows may indicate that star formation and feedback has taken place in the recent past, in a way that these outflows could develop.

During the last two decades, significant progress was achieved in our understanding of the distribution and physical properties of circumgalactic and intergalactic gas in the Local Group (hereafter LG; e.g., Wakker & van Woerden 1997; Richter 2006; Putman et al.

2012, for reviews on this topic). Recent observational campaigns including 21 cm radio observations of neutral hydrogen (e.g., Thilker et al. 2004; Kalberla & Haud 2006; Kerp et al. 2011), and absorption-line measurements of neutral and ionized gas in the optical and ultraviolet (UV; e.g., Sembach et al. 2003; Collins et al. 2005, 2009; Ben Bekhti et al. 2008, 2012; Richter et al. 2009, 2012 [hereafter R12]; Herenz et al. 2013; Rao et al. 2013) indicate the extreme multi-phase character of circumgalactic gas within the virial radii of the Milky Way and Andromeda galaxies. One major difficulty in disentangling the various gaseous components in the LG and constraining their origin and fate lies in the fact that the three-dimensional distribution of the gas is very difficult to establish from our perspective within the Milky Way. This is because direct distance estimates of circumgalactic gas complexes are very difficult to obtain, as they require a large observational effort (Wakker et al. 2007, 2008).

\* snuza@aip.de

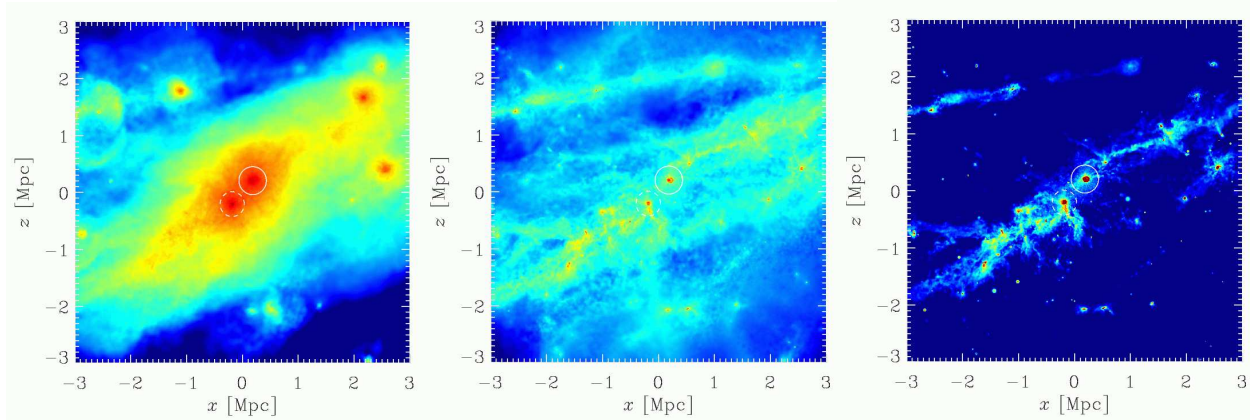


**Figure 1.** Gas density maps of the simulated LG at  $z = 0$  for the hot ( $T \geq 10^5$  K; left-hand panel), cold ( $T < 10^5$  K; middle panel) and H I (right-hand panel) components. The plots are centred in the MW<sup>c</sup>/M31<sup>c</sup> system. The virial radii of our Milky Way and Andromeda candidates are shown as dashed and solid lines respectively. In order to highlight the differences in the distribution of the hot, cold and neutral gas components, each plot shows the projected density in a color scale covering four orders of magnitude.

Our current understanding is that the Milky Way and Andromeda, the two major spiral galaxies in the LG, are both surrounded by multi-phase gas halos, whose properties reflect the various processes that circulate gaseous material in their circumgalactic environments (i.e., outflows, inflows and tidal interactions). Observations imply that the cold ( $T < 10^4$  K), and predominantly neutral, circumgalactic gas that gives rise to detectable H I 21 cm emission appears to be concentrated within a distance of  $\sim 50$  kpc from the Milky Way and Andromeda galaxies (Thilker et al. 2004; Wakker et al. 2007, 2008; Richter 2012). At larger distances, and even beyond the virial radii of the two galaxies, the LG is possibly filled with highly ionized, hot ( $T \gtrsim 10^5$  K) gas that gives rise to absorption of highly-ionized oxygen in the UV (O VI Sembach et al. 2003) and in the X-ray band (O VII and O VIII; Gupta et al. 2012) in the spectra of distant quasars, blazars and other UV and X-ray bright background sources. It is therefore possible that this warm-hot circumgalactic medium harbours a large fraction of the baryons present in the LG, which could explain the apparent discrepancy between the baryon content found in galaxy groups and the mean cosmological value (see also Richter et al. 2008). This line of evidence is strengthened by the recent discovery of X-ray haloes surrounding regular, although massive, spiral galaxies that are not related to merger interactions, starbursts and/or emission from compact objects (Anderson & Bregman 2011; Dai et al. 2012; Bogdán et al. 2013a,b).

According to the standard picture of galaxy formation, two main accretion modes are responsible for feeding galaxies with a fresh supply of cold gas that can be further processed into stars: a ‘hot’-mode, originated as high-density gas surrounding the galaxy cools radiatively and collapses towards the centre (e.g., White & Rees 1978), and a ‘cold’-mode, driven by cold gas filaments penetrating well inside the virial radius of the halo (e.g., Navarro & Steinmetz 1997; Kereš et al. 2005).

Recently, several authors have studied the distribution of gas, and their associated accretion modes, for isolated galaxy haloes using cosmological simulations. For instance, Fernández et al. (2012) focused on the cold accretion mode

in an isolated Milky Way-mass galaxy with low velocity dispersion under the condition that the mean environmental density at  $z = 0$  is close to that of the actual LG. Similarly, Joung et al. (2012) extended this work by considering the accretion of warm-hot material onto the halo. Their results indicate that the accretion rate in the system is dominated by ionized warm-hot gas over a large range of distances extending up to the virial radius, whereas cooler gas tends to occupy the central regions.

In this work, we study the properties of gas in a constrained simulation of the LG of galaxies, therefore including the interaction between their members, and make detailed comparisons with available observations. Our simulation reproduces the local environment of the LG, going beyond the simple criteria adopted by Fernández et al. (2012), while including the main observed large scale structures that surround the LG (e.g., the Virgo cluster among other mass aggregations). The simulated LG contains two main galaxies that, at  $z = 0$ , approximately resemble the Milky Way and Andromeda galaxies in terms of their masses, separation, relative velocity and orientation of the discs. Our aim is to characterize the spatial distribution and physical conditions of the different gas phases in the simulated LG, as well as to compare these results with recent multi-wavelength observations of gas in the circumgalactic environment of the Milky Way and Andromeda. In a companion paper (Scannapieco et al. 2014) we study the formation of the Milky Way and Andromeda candidates in the same simulation, but focusing on the evolution of stellar discs and their merger histories in relation to the environment.

Our paper is organized as follows: in Section 2 we describe the main aspects of the simulation and simulated LG; in Section 3 we analyse the properties of the gas at the largest scales of the LG, as well as within the simulated Milky Way and Andromeda haloes. In Section 4 we compare the distribution of hot, cold and neutral gas belonging to the galaxies with observations and discuss how well the covering fractions of neutral hydrogen compare with observational results in the Milky Way and Andromeda. In Section 5, we discuss accretion and ejection rates of gas onto

the main LG haloes, and in Section 6 we analyse the gas distribution around the simulated Milky Way/Andromeda system. In Section 7, we compare some of our findings with previous work and in Section 8 we present our conclusions.

## 2 THE CONSTRAINED COSMOLOGICAL SIMULATION

This study is carried out within the context of the Constrained Local UniversE Simulations (CLUES) project ([www.clues-project.org](http://www.clues-project.org)) which aims at simulating a realistic LG including the effects of the local environment as well as of the most prominent surrounding structures.

The initial conditions (ICs) are constructed using the Hoffman-Ribak algorithm (Hoffman & Ribak 1991) as a way to impose a set of Gaussian constraints at high redshift using a number of observational constraints at  $z \approx 0$ . The initial matter distribution consists of a cubic box of  $64 h^{-1}$  Mpc side length which contains a high-resolution spherical region of  $2 h^{-1}$  Mpc radius located at its centre.

The simulation contains structures resembling the Virgo, Great Attractor, Fornax and Perseus clusters (see e.g., Klypin et al. 2003). Since typical constraints are of the order of a few Mpc, structure formation at the smallest scales is essentially random. For this reason, a series of realizations were run in order to get the best possible match of our Milky Way and Andromeda galaxy candidates with the available estimates of masses and relative radial velocity of the LG galaxies. Further details on the generation of ICs can be found in Gottlöber et al. (2010).

The simulation was started at a redshift of  $z = 50$  assuming a  $\Lambda$ CDM cosmology (WMAP5). For the cosmological parameters we adopted a matter density of  $\Omega_m = 0.279$ , a baryon density of  $\Omega_b = 0.046$ , a cosmological constant density of  $\Omega_\Lambda = 0.721$ , a Hubble constant of  $100h$  km s $^{-1}$  Mpc $^{-1}$  with  $h = 0.7$ , and a power spectrum normalization of  $\sigma_8 = 0.8$ . The mass of the gas and dark matter particles inside the high-resolution sphere is  $M_g = 3.89 \times 10^5 h^{-1} M_\odot$  and  $M_{dm} = 1.97 \times 10^6 h^{-1} M_\odot$  respectively. The interested reader is referred to Scannapieco et al. (2014) for further details on this simulation.

To identify (sub)structures in the simulation, we use the halo finder SUBFIND (Springel et al. 2001; Dolag et al. 2009). This code allows to link each particle in the simulation (gas, stars and dark matter) to a given substructure (containing a minimum of 32 particles) based on its binding energy. In this way, it is possible to identify the main haloes within the simulation at each redshift as well as their associated satellite systems.

### 2.1 The Simulation Code

For this study, we use the Smoothed Particle Hydrodynamics (SPH) simulation code GADGET3 (Springel et al. 2008) with the extensions of Scannapieco et al. (2005, 2006). The code includes metal-dependent cooling (above  $10^4$  K; Sutherland & Dopita 1993) and chemical enrichment, a multiphase model for the gas component and supernova (thermal) feedback. We refer the interested reader to Scannapieco et al. (2005, 2006) for details on the implementation of these processes.

The multiphase and feedback models naturally generate galactic winds after significant star formation bursts (Scannapieco et al. 2006, 2008). This feature allows to study in a more realistic manner the distribution of gas in and around haloes, as well as in the intergalactic medium, since there is no a priori assumption on the occurrence and/or strength of the winds. Moreover, since the code follows the enrichment of the interstellar medium from supernova Type Ia and Type II explosions, it is possible to investigate the chemical properties of the gas component in the simulation and, in particular, the distribution of the H I gas.

The Scannapieco et al. model has been successfully applied to the study of Milky Way-mass galaxies (Scannapieco et al. 2009, 2010, 2011) and of dwarf spheroidal galaxies (Sawala et al. 2011, 2012). Particularly relevant for this study is that the same input parameters are used in the aforementioned studies, indicating that the code can properly follow the formation of systems of different mass. This is possible because the implementation of supernova feedback, whose effects strongly depend on the mass of a system, has been specifically designed to avoid the introduction of scale-dependent parameters (see Scannapieco et al. 2006, 2008). The ability to simulate different mass systems with the same choice of input parameters is of relevance in cosmological simulations, where systems of all masses are forming simultaneously at any time.

Recently, there has been considerable discussion on the ability of the SPH technique to capture some small-scale processes, particularly fluid mixing and jumps in physical properties (see e.g. Agertz et al. 2007; Read & Hayfield 2012; Hopkins 2013 and references therein). We do not expect these problems to be particularly severe in our simulation. On one hand, SPH gives accurate gas properties in the intergalactic medium, where the gas is at relatively low densities and there is no significant spatial coexistence of different phases. Within the haloes, the gas has a complex multi-phase structure, that standard SPH might not be able to accurately resolve. However, our multi-phase model has proven efficient at describing the coexistence of gas at different phases (Scannapieco et al. 2006), and therefore we do not expect our results to be strongly affected by numerical problems connected to the SPH technique.

We note that our simulation does not include the effects of radiation pressure (RP) provided by massive stars prior to supernova explosions, a process that has been included only very recently in cosmological simulations (e.g., Stinson et al. 2013; Aumer et al. 2013). These works found that RP efficiently regulates star formation, particularly at high redshift, producing halo-to-stellar mass relations in better agreement with the predictions of abundance matching models. RP affects mainly the central regions of haloes, but should not strongly affect the global properties of the gaseous haloes or intergalactic medium.

### 2.2 The simulated Local Group

The simulated LG at the present time includes two main massive haloes within the  $2 h^{-1}$  Mpc high-resolution region that can be associated to the Milky Way and Andromeda galaxies. In what follows, we will refer to our simulated galaxy candidates using a ‘c’ superscript, i.e. MW<sup>c</sup> and M31<sup>c</sup> respectively, while keeping the names Milky Way and An-

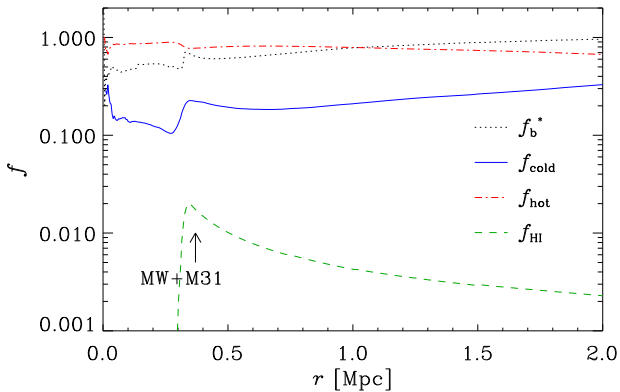


**Figure 2.** Fraction of cold gas ( $f_{\text{cold}}$ ; solid line), hot gas ( $f_{\text{hot}}$ ; dot-dashed line), H I gas ( $f_{\text{HI}}$ ; dashed line) and baryons ( $f_{\text{b}}^*$ , normalized to the universal baryon fraction; dotted line) for increasingly larger spheres centred in the MW<sup>c</sup>/M31<sup>c</sup> system. The arrow indicates the position of the MW<sup>c</sup> and M31<sup>c</sup> galaxies.

dromeda for reference to the actual systems and related observational quantities. Note that, as stated above, the simulation does not allow to directly constrain the properties at galaxy-size scales, and thus the two simulated galaxies have dynamical and kinematical properties that can only approximate those of the actual Milky Way and Andromeda.

As in the real LG, M31<sup>c</sup> and MW<sup>c</sup> are approaching each other. The relative radial velocity between the mass centres of the simulated galaxies is  $-138 \text{ km s}^{-1}$ , a value which is close to the recent observational estimate of  $-109.3 \pm 4.4 \text{ km s}^{-1}$  for the Andromeda and Milky Way system presented by van der Marel et al. (2012). On the other hand, the distance between M31<sup>c</sup> and MW<sup>c</sup> is 652 kpc, in comparison to the observed value of  $770 \pm 40 \text{ kpc}$  (e.g., Ribas et al. 2005).

Observational estimates of both the Milky Way and Andromeda virial masses range from about  $10^{12} M_{\odot}$  to  $2.5 \times 10^{12} M_{\odot}$  (van der Marel et al. 2012, and references therein). To compute the virial mass of the simulated galaxies we rely on the definition of the virial radius, noted  $R_{\text{vir}}$ , as the one comprising a mass density 200 times that of the critical density of the universe. As a result, the simulated M31<sup>c</sup> and MW<sup>c</sup> systems have virial masses of  $1.68 \times 10^{12} M_{\odot}$  and  $1.23 \times 10^{12} M_{\odot}$  respectively, where we have decided to take the less massive system as the Milky Way candidate.

The uniqueness of our constrained simulation is that it comprises two massive Milky Way-mass galaxies located in a large-scale environment that reproduces the distribution of the most massive structures of the local Universe. As an additional characteristic, the resulting orientations of the gaseous galaxy discs at  $z = 0$  resemble those of the real Milky Way and Andromeda galaxies as it will be shown in Section 4.4.

In Table 1 we present some of the global properties of the simulated LG massive galaxies including virial mass, virial radius, virial velocity and total dark matter and gas masses within the virial radius.

**Table 1.** Main properties of the M31<sup>c</sup> and MW<sup>c</sup> simulated haloes: virial mass, virial radius, virial velocity, and total dark matter and gas masses. The latter correspond to values within the virial radius as defined in Section 2.2. Masses, radii and velocities are given in units of  $10^{10} M_{\odot}$ , kpc and  $\text{km s}^{-1}$ , respectively.

	$M_{\text{vir}}$	$R_{\text{vir}}$	$V_{\text{vir}}$	$M_{\text{DM}}$	$M_{\text{gas}}$
M31 <sup>c</sup>	167.9	244.9	171.9	153.3	6.7
MW <sup>c</sup>	125.1	222.2	155.8	113.1	5.7

### 3 GENERAL PROPERTIES OF THE GAS WITHIN THE LOCAL GROUP

In this section, we discuss some basic properties of the gas within the LG, as well as in the MW<sup>c</sup> and M31<sup>c</sup> haloes at  $z = 0$ . We first give a general description of the large-scale environment where MW<sup>c</sup> and M31<sup>c</sup> reside to later discuss these systems in more detail.

#### 3.1 Large-scale environment

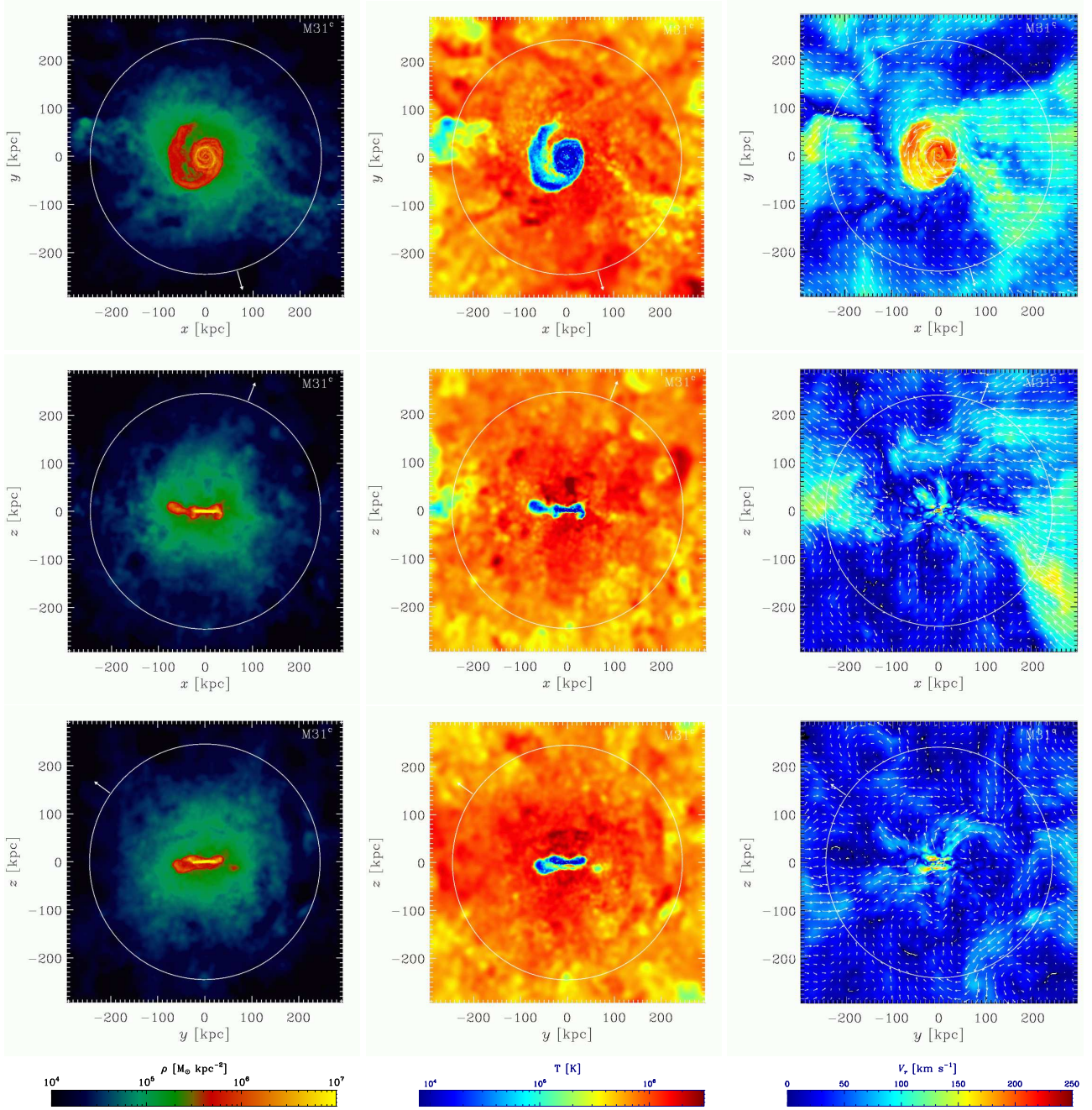
We first focus our attention on the large-scale environment where our MW<sup>c</sup> and M31<sup>c</sup> candidates reside. Throughout this work we adopt a simple criterium to separate gas among cold and hot phases: a temperature threshold of  $10^5 \text{ K}$ . We also study the neutral gas component in terms of its H I content. At every time, we solve for the amount of H I assuming ionization equilibrium for all hydrogen and helium species including photoionization by a radiation background that accounts for the integrated UV field of external sources. In this work, we do not consider radiation generated by stars belonging to our simulated galaxies.

Fig. 1 shows one projection of the gas density distribution for the hot, cold and H I gas components in a box of 6 Mpc on a side centred in the location of the simulated LG. The virial radii of our MW<sup>c</sup> and M31<sup>c</sup> galaxy candidates are indicated as small circles (dashed and solid lines respectively). As expected, the cold gas phase (middle panel) displays a more filamentary structure than the more diffuse, hot component (left-hand panel). The gas density distribution of H I is shown in the right-hand panel. The distribution of neutral gas is much more concentrated, being mainly located within the very centres of the MW<sup>c</sup> and M31<sup>c</sup> haloes, and also in individual complexes in the intergalactic medium not related to satellite galaxies. We analyse in more detail the H I distribution around the MW<sup>c</sup> and M31<sup>c</sup> galaxies in Section 4.

From our simulation we can easily evaluate the fraction of gas in the different components within the simulated LG. This can be seen in Fig. 2 where we plot the fraction of hot, cold and H I gas as a function of distance to the geometrical centre of the MW<sup>c</sup>/M31<sup>c</sup> system. For the sake of completeness, we also show the baryon fraction normalized to the universal value. As expected, fluctuations are higher for the smallest scales as a result of the clumpiness of matter aggregations. The features located at  $\sim 300 \text{ kpc}$  are owing to the presence of the MW<sup>c</sup> and M31<sup>c</sup> galaxies which increase (decrease) the fraction of cold (hot) gas.

At dynamically relevant distances for the MW<sup>c</sup>-M31<sup>c</sup> interacting system the hot component dominates the gas





**Figure 3.** Face-on (upper panels) and edge-on (middle and lower panels) maps of gas density, temperature and projected velocity with respect to centre of mass of the simulated M31<sup>c</sup>. For the latter, the colours represent the absolute magnitude of the corresponding velocity and the arrows show the direction of the velocity field at each position. For the gas density, we include all mass within a cubic box of  $1.2 \times R_{\text{vir}}$  on a side. In the case of temperatures and velocities, the plots are also  $1.2 \times R_{\text{vir}}$  on a side, but include only mass within thin slices  $0.24 \times R_{\text{vir}}$  wide. The circles indicate the location of the virial radius and the arrows point towards the position of the MW<sup>c</sup>.

mass as expected for merging haloes. At a scale of 1 Mpc the hot gas fraction reaches a value of  $\sim 80\%$ . For larger distances, the hot gas fraction decreases slightly as the fraction of cold gas increases reaching a value of about 30% at a radius of 2 Mpc. These results indicate that a considerable fraction of the mass in the LG is most likely in the form of a large, difficult to detect, hot gas reservoir. In Section 4 we will focus on the mass content of hot gas within the haloes of

our MW<sup>c</sup> and M31<sup>c</sup> candidates and their comparison with observations.

As mentioned above, we also evaluated the baryon fraction of our simulated LG as a function of distance. Interestingly, for a typical LG radius of 2 Mpc, we found that the baryon fraction has almost converged to the universal value, while at smaller distances it is slightly lower. For instance, if we evaluate the baryon fraction at a distance of 1 Mpc, which already comprises the two main members of

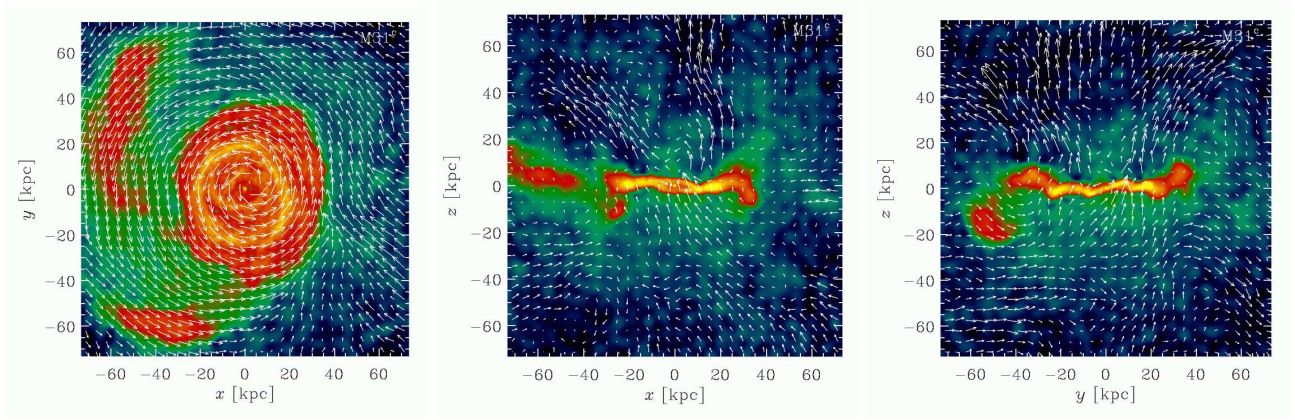


**Figure 4.** Zoom in of the projected gas density for M31<sup>c</sup>, within the inner  $0.3 \times R_{\text{vir}}$ , and corresponding velocity field (arrows). The color scale is the same than that of Fig. 3.

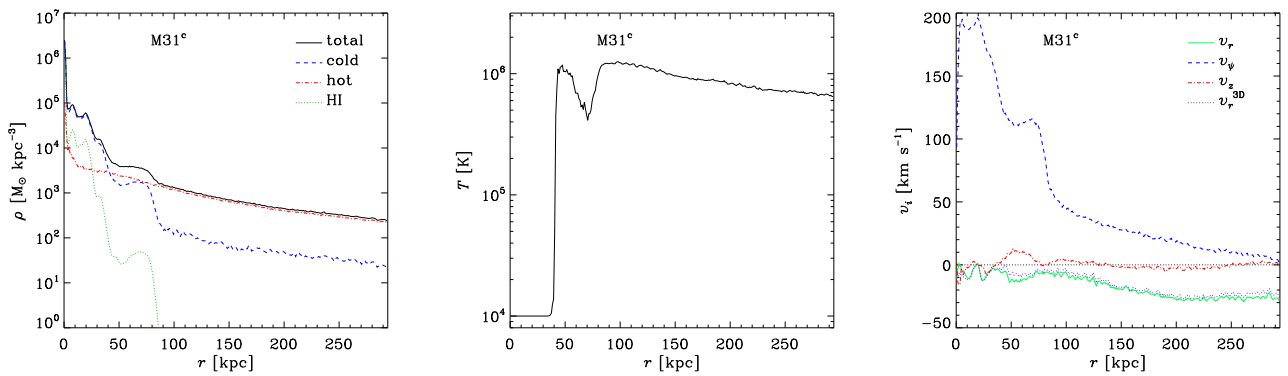


**Figure 5.** Density, temperature and velocity profiles for M31<sup>c</sup>, up to  $1.2 \times R_{\text{vir}}$ . For the density, we show also the profiles of the hot ( $T \geq 10^5$  K, dotted-dashed line), cold ( $T < 10^5$  K, dashed line) and H I (dotted line) gas separately. In the case of the velocities, we show the profiles of radial (solid green line), tangential (dashed blue line) and vertical (dot-dashed red line) velocity in a cylindrical coordinate system. Furthermore, for the vertical velocity, we show  $V_z^* \equiv v_z \text{sign}(z)$  in order to easily differentiate between inflows ( $V_z^* \leq 0$ ) and outflows ( $V_z^* > 0$ ).

the LG, the MW<sup>c</sup> and M31<sup>c</sup>, the baryon fraction is roughly  $\sim 20\%$  smaller than the universal value showing that cosmic variance plays a role at Mpc scales.

In the next two sections we turn our attention to the two main simulated galaxies within the LG. For each galaxy we rotate the system of reference in order to align the total angular momentum of the gas (within the inner 30 kpc) with the  $z$ -direction. In this way, projecting the systems in the  $xy$  plane will result in a face-on view, while doing so in the  $xz$  or  $yz$  planes will correspond to the edge-on views.

### 3.2 Andromeda galaxy candidate

In Fig. 3 we show the face-on (upper panels) and edge-on (middle and lower panels) maps of density and temperature for the simulated M31<sup>c</sup>. The right-hand panels show the corresponding projected velocity field, in absolute value (colours) and direction (arrows). We plot peculiar velocities with respect to the corresponding centre of mass velocity. The plots cover a cubic region of 1.2 times the virial radius

of M31<sup>c</sup> which is indicated by the circles. For every projection, arrows point in the direction towards the MW<sup>c</sup> galaxy.

From the density and temperature plots, we can see that the simulated M31<sup>c</sup> system has an extended disc<sup>1</sup> of cold gas, and a more diffuse hot gas halo. The disc is thin and it shows the presence of an extended spiral arm-like feature which has a slightly higher temperature than the typical  $10^4$  K of the disc. We also see that some of the gas around the disc, in particular at positive values of the  $z$  component in the edge-on views, has slightly higher temperature than the halo gas in the immediate vicinity. This is owing to supernova feedback, which heats up gas and drives winds, mainly in directions perpendicular to the disc (see Scannapieco et al. 2006).

As a result of the combined and complex effects of cooling and supernova heating, the gas distributions in the most

<sup>1</sup> This simulated galaxy does show a prominent stellar disc up to  $z \approx 0.3$ , which is significantly reduced at  $z = 0$  as a result of the interaction with 2 intermediate-mass satellites. For more details see Scannapieco et al. (2014).



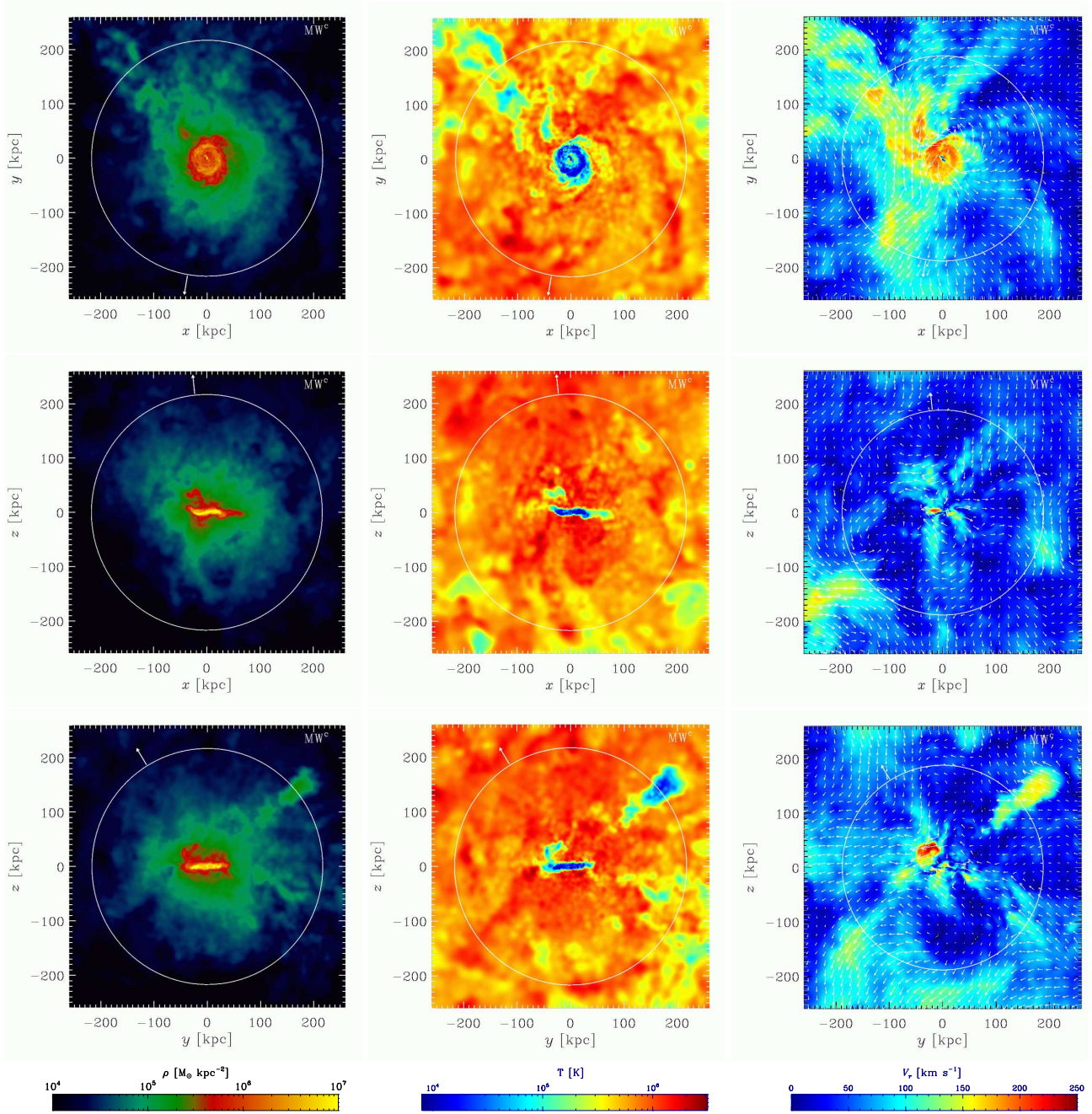


**Figure 6.** Face-on (upper panels) and edge-on (middle and lower panels) maps of gas density, temperature and projected velocity with respect to centre of mass of the simulated MW<sup>c</sup> (idem as Fig. 3 but for the MW<sup>c</sup> case). The circles indicate the location of the virial radius and the arrows point towards the position of M31<sup>c</sup>.

central regions of the simulated M31<sup>c</sup> show significant asymmetries. This can be better seen from Fig. 4, where we show zoom-in versions of the projected density of M31<sup>c</sup>, together with the velocity field (arrows). The rotation of the gas is clearly seen in the face-on view, while important supernova-driven outflows are present, particularly in the positive  $z$ -axis region.

We found that some of the gas in the halo of M31<sup>c</sup> is flowing in, as can be seen from the right-hand panels of Fig. 3. In particular, inflowing gas with a velocity of  $\sim 100$  km s<sup>-1</sup> is seen coming from outside the virial radius all the

way down to the galactic disc. In the central regions, however, there are important outflows, as already evident from Fig. 4. In general, the gas velocity structure is complex and extremely asymmetric, as expected in a cosmological context where both internal (i.e., star formation and supernova feedback) and external (e.g., gas accretion, interactions and mergers) effects shape the gas distribution in a non-trivial manner.

Fig. 5 shows the spherically-averaged gas density, temperature and velocity profiles for the simulated M31<sup>c</sup>. The density profile is split into the hot ( $T \geq 10^5$  K), cold (other-

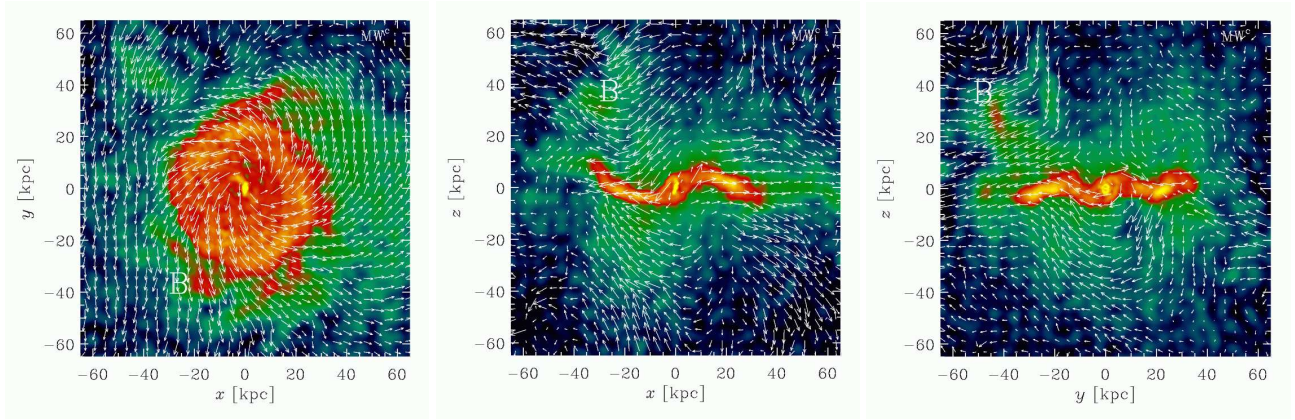


**Figure 7.** Zoom in of the projected gas density for  $MW^c$ , within the inner  $0.3 \times R_{\text{vir}}$ , and corresponding velocity field (arrows). The color scale is the same as that of Fig. 6. See section 4.4.1 for reference of label “B”.

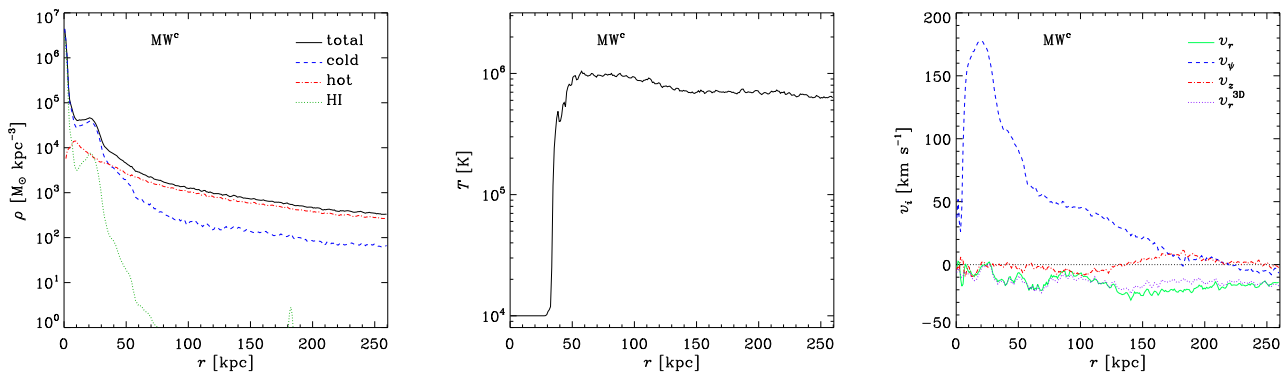


**Figure 8.** Density, temperature and velocity profiles for the  $MW^c$ , up to  $1.2 \times R_{\text{vir}}$  (idem as Fig. 5 but for the  $MW^c$  case).

wise), and neutral gas components. As can be seen from the left-hand panel, the density increases significantly within the disc region, has a slight increase owing to the spiral arm-like feature located at a distance of about 60 kpc, and declines smoothly for larger radii.

As expected, in the central region, the material is mainly star-forming, cold gas, while outside the disc it is in a hot, diffuse phase. This can be seen in the middle panel of Fig. 5 where we show the temperature profile of the gas. The gas disc has a temperature of  $10^4$  K, with a typical extent of about 40 kpc. For larger scales the temperature increases very quickly up to about  $10^6$  K staying pretty much constant through the hot gas halo (the drop in temperature between 50 – 70 kpc is indicative of the arm-like feature discussed earlier). As for the neutral gas, it is the most concentrated component, and declines very steeply after  $r \sim 70$  kpc.

The gas velocity profile can be seen in the right-hand panel of Fig. 5 where we show the profiles of radial, tangential and vertical velocity as measured in a cylindrical coordinate system. For the vertical velocity, we adopt  $V_z^* \equiv v_z \text{sign}(z)$  to easily differentiate between inflow ( $V_z^* \leq 0$ ) and outflow ( $V_z^* > 0$ ) gas velocities. As expected, the gas velocity in the disc region is dominated by the tangential component, where the bump observed at  $\sim 60$  kpc is related to the spiral arm-like feature described before. For distances

approaching the virial radius, tangential velocity decreases indicating that the rotational support is not significant at these larger radii. Furthermore, we can see that, in the disc plane, there is a net radial infall of gas which, however, has a small velocity, of the order of  $10 \text{ km s}^{-1}$  in the central region and reaching about  $30 \text{ km s}^{-1}$  near the virial radius.

### 3.3 Milky Way galaxy candidate

Now we turn our attention to the simulated  $MW^c$  system. As explained above,  $MW^c$  is slightly less massive than  $M31^c$ , but we expect a similar behaviour of the gas, specially in the halo region. Fig. 6 shows the face-on (upper panels) and edge-on (middle and lower panels) projections of density, temperature and projected velocity for the simulated  $MW^c$ . In these plots, the colour scale for each quantity is the same than that used for  $M31^c$ , in order to highlight the possible differences and similarities of the two galaxies.

As we found for  $M31^c$ , the simulated  $MW^c$  system also has a disc<sup>2</sup> of cold, dense gas. In this case, no large spiral

<sup>2</sup> The associated stellar disc has a radius of about 12 kpc and a mass of  $2.83 \times 10^{10} M_{\odot}$  according to the kinematical decomposition method. For more details see Scannapieco et al. (2014).



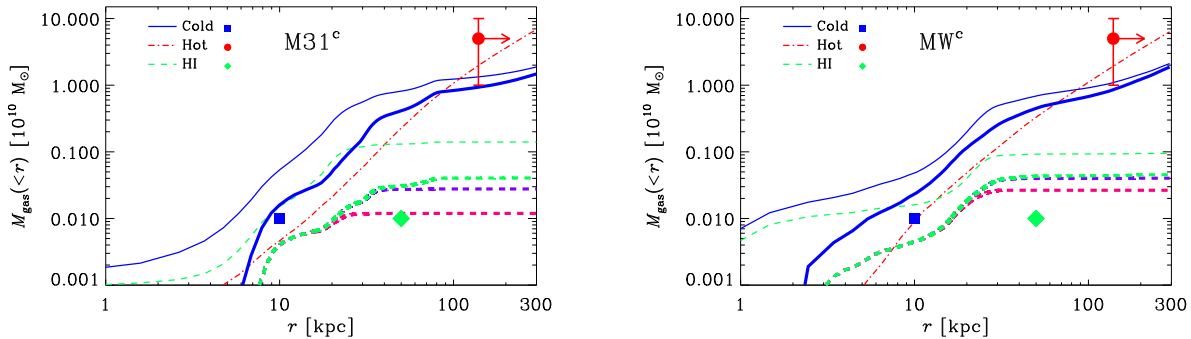


**Figure 9.** Cumulative mass profiles of different gas components (i.e., cold, hot and H I) for the M31<sup>c</sup> and MW<sup>c</sup> simulated galaxies (left- and right-hand panels respectively). The cold and H I contributions excluding the gaseous disc are shown as thicker lines. In the case of H I we also plot the cumulative mass profiles for column density limits of  $N_{\text{HI}} \geq 10^{19} \text{ cm}^{-2}$  (blue dashed lines) and  $N_{\text{HI}} \geq 10^{20} \text{ cm}^{-2}$  (magenta dashed lines) excluding the gaseous disc. Symbols show Milky Way gas-mass estimates from observations for material within 10 kpc (cold; see e.g. Shull et al. 2009; Lehner & Howk 2011), 50 kpc (H I; see Richter 2012) and 139 kpc (hot; see Gupta et al. 2012). In the latter, the arrow indicates a lower-limit distance.

arms are seen, but we do observe a significant asymmetry in the gas density, evident in both the face-on and edge-on maps, specially near the disc region. The temperature distribution is extremely complex; although most of the gas in the halo is at temperatures close to  $T \sim 10^6 \text{ K}$ , there are regions with somewhat colder temperatures. The most salient features in our simulated MW<sup>c</sup> are the presence of a relatively large region of significant accretion of  $\sim 10^5 \text{ K}$  gas (to the upper-left direction in the face-on view), and a more localized accretion region to the upper-right corner in the  $yz$  view near the virial radius. The typical velocities of these inflows are  $\sim 100\text{--}150 \text{ km s}^{-1}$ .

From the right-hand panels of Fig. 6, we can observe a high degree of complexity, as we have seen for M31<sup>c</sup>. Again, most of the gas is inflowing, except for a few regions dominated by supernova outflows. Fig. 7 shows a zoom-in in the disc region of the MW<sup>c</sup>, where the left-hand panel shows a face-on view, while the middle- and right-hand panels show edge-on views. From the edge-on projections, it is clear that the gas disc, instead of showing the usual rectangular-like shape, presents some asymmetries. The disc is also not fully symmetric in the outer disc regions, as particularly evident in the face-on view (left-hand panel), at  $x > 40 \text{ kpc}$ . As in M31<sup>c</sup>, such complexity is the result of the non trivial interplay between the different physical processes (cooling, heating, exchange of gas between the halo and the intergalactic medium) involved in the assembly of  $\Lambda\text{CDM}$  galaxies.

Fig. 8 shows the spherically-averaged profiles of gas density (left-hand panel), temperature (middle panel) and velocity (right-hand panel) for the MW<sup>c</sup>. In this case, the gas disc is smaller in extent, reaching a radius of  $\sim 30 \text{ kpc}$ . The neutral gas is, as we found for M31<sup>c</sup>, the most concentrated component. The gas temperature at the disc is of about  $10^4 \text{ K}$ . At larger distances, it peaks at  $\sim 10^6 \text{ K}$  to gradually decrease to about  $6 \times 10^5 \text{ K}$  near the virial radius. As before, the velocity of gas belonging to the disc is dominated by their tangential components, reaching similar velocity values than those found for M31<sup>c</sup>. However, contrary to the case of M31<sup>c</sup>, we detect slightly higher vertical velocities in comparison. More importantly, we found that the radial velocities

are negative with absolute values ranging from  $10\text{--}20 \text{ km s}^{-1}$  near the disc edges, and up to  $20\text{--}30 \text{ km s}^{-1}$  in the halo. This indicates the presence of radial gas infall that occurs mainly in the galactic disc plane.

#### 4 HOT, COLD AND NEUTRAL GAS PHASES: COMPARISON WITH OBSERVATIONS

We have so far discussed the general distribution and properties of the gas within the simulated MW<sup>c</sup> and M31<sup>c</sup> haloes. In this section, we study the different gas phases present in the simulation (i.e., cold, hot or H I) and compare our results with available observations. As mentioned before, we use a simple threshold temperature of  $10^5 \text{ K}$  to separate gas among cold and hot phases. Additional information of our simulations is the amount of neutral hydrogen, which is a useful quantity to compare with observations given the large amount of available 21 cm data.

The cumulative mass profiles of the different gaseous components of our two simulated galaxies, together with observational estimates for the hot, cold and H I gaseous phases in the Milky Way, are shown in Fig. 9. Additionally, Table 2 shows the amount of gas in the different phases for the MW<sup>c</sup> and M31<sup>c</sup> within several radii; results are presented for the virial radius, as well as for 10 kpc, 50 kpc and 100 kpc from the centre, respectively. These scales enable us to compare our results with observations in a more consistent way.

##### 4.1 Warm-hot gaseous haloes

Recent observations have allowed to estimate a number of quantities related to the amount and nature of the gas within the haloes of the Milky Way and Andromeda galaxies (Sembach et al. 2003; Gupta et al. 2012). In particular, studying the X-ray absorption features of O VI and O VII, Gupta et al. (2012) inferred the presence of a large warm-hot gas reservoir surrounding the Milky Way, with a temperature  $T \gtrsim 10^6 \text{ K}$ . These authors also give an estimate of the amount of mass in this warm-hot phase traced by O VII

**Table 2.** Total mass of cold, hot and H I gas of the simulated M31<sup>c</sup> and MW<sup>c</sup> galaxies within different radii  $R$ . We also show the gas mass in the different components within 10 kpc and 50 kpc, but excluding the disc region. Additional column density cuts are considered in the H I case. All masses are given in units of  $10^8 M_\odot$ .

Radius (kpc)	$M_{\text{cold}}(\leq R)$		$M_{\text{hot}}(\leq R)$		$M_{\text{HI}}(\leq R)$		$M_{\text{HI}}(\leq R)^\dagger$		$M_{\text{HI}}(\leq R)^\ddagger$	
	M31 <sup>c</sup>	MW <sup>c</sup>	M31 <sup>c</sup>	MW <sup>c</sup>	M31 <sup>c</sup>	MW <sup>c</sup>	M31 <sup>c</sup>	MW <sup>c</sup>	M31 <sup>c</sup>	MW <sup>c</sup>
10	4.84	4.59	0.41	0.76	1.38	1.58	1.38	1.58	1.38	1.58
10 (no disc)	1.42	2.16	0.27	0.56	0.40	0.45	0.40	0.45	0.40	0.45
50	81.07	68.33	22.04	32.32	13.06	9.21	12.71	8.90	10.03	6.44
50 (no disc)	40.97	44.48	21.44	30.84	3.08	4.09	2.73	3.98	1.19	2.65
100	123.26	91.22	106.09	109.60	14.01	9.30	12.75	8.90	10.03	6.44
$R_{\text{vir}}$	166.56	159.45	499.19	408.94	14.04	9.45	12.75	8.90	10.03	6.44

$$^\dagger N_{\text{HI}} \geq 10^{19} \text{ cm}^{-2}, \quad ^\ddagger N_{\text{HI}} \geq 10^{20} \text{ cm}^{-2}$$

absorbers in the Milky Way, which is  $M_{\text{hot}} \gtrsim 6.1 \times 10^{10} M_\odot$ . This estimate, however, strongly depends on several model assumptions, such as the metallicity of the gas and the O VII ionization fraction, and thus should be interpreted with caution. The value given above corresponds to a path-length of  $l > 139$  kpc, where the oxygen solar abundance of Anders & Grevesse (1989) was used. Adopting newer estimates of the oxygen solar abundance results in even larger path-lengths, thus decreasing the lower bound for the mass of the Milky Way hot gaseous halo. For instance, the use of the Asplund et al. (2009) oxygen solar abundance results in an estimate of  $M_{\text{hot}} \gtrsim 1.2 \times 10^{10} M_\odot$  (see Mathur 2012, for a discussion of the different assumptions involved in these kind of estimations). Results of other researchers also support values for the total mass of the Milky Way hot coronal gas in the range  $M_{\text{hot}} = 10^{10} - 10^{11} M_\odot$  (e.g., Fang et al. 2013). However, we note that not all authors agree with these scalings for the size and mass of the Milky Way’s hot gaseous corona. For a critical discussion concerning this point see e.g. Collins et al. (2005), Bregman (2007), Yao et al. (2008) and Anderson & Bregman (2010).

As shown in the previous section, the haloes of our simulated MW<sup>c</sup> and M31<sup>c</sup> systems, in particular at distances greater than  $\sim 50$  kpc, have temperatures close to  $10^6$  K (middle panels of Figs. 5 and 8). Fig. 9 shows the cumulative mass profile of the hot ( $T \geq 10^5$  K) component of our simulated galaxies (dot-dashed lines). When we consider all the gas up to the virial radius, we found that the cumulative mass is  $M_{\text{hot}} \approx 5 \times 10^{10} M_\odot$  and  $4.1 \times 10^{10} M_\odot$  for M31<sup>c</sup> and MW<sup>c</sup>, respectively (see Table 2). These values are similar to the observational estimates discussed above. If we consider only gas enclosed within 100 kpc the resulting gas masses lower to  $\sim 1.1 \times 10^{10} M_\odot$  for both simulated galaxies. These quantities are again of the same order of magnitude than the observational estimates corresponding to the Milky Way.

## 4.2 Cold-warm gas component

Observations of circumgalactic gas with temperatures below  $\sim 10^5$  K may occur either as a diffuse, ionized medium, or as a neutral one. The neutral gas fraction in these structures is too small for the H I line to be detected, however, their neutral hydrogen content can be estimated from the analysis of the H I Lyman series absorption (e.g., Richter et al. 2009). In our simulation, we found that most of the material cor-

responding to the cold gas component is mainly composed of ionized gas, in agreement with observational studies.

Diffuse, ionized gas in the extended Milky Way halo has been studied in UV absorption of intermediate and high ions of carbon, silicon, and other elements (e.g., C III, C IV, Si III, Si IV). UV observations with FUSE and HST/STIS indicate that the warm ionized gas in the Milky Way halo comes in individual gas complexes and coherent structures, thus similar as those found for H I structures (see, e.g., Collins et al. 2009; Shull et al. 2009; Winkel et al. 2011; Lehner et al. 2012; Herenz et al. 2013). Such diffuse, ionized halo structures have large sky covering fraction of more than 70 percent (Shull et al. 2009; Herenz et al. 2013), suggesting that this gas phase is widespread and it may harbour a significant fraction of the gas mass with  $T < 10^5$  K in the Milky Way halo.

Shull et al. (2009) and Lehner & Howk (2011) estimated a total mass of this warm, ionized gas component in the Milky Way halo, of  $\sim 10^8 M_\odot$  at a distance of  $\sim 10$  kpc above the galactic plane. As for the coronal gas, it has to be noted, however, this estimate depends critically on the (uncertain) ionization conditions and the chemical composition of the gas and thus must be regarded as a rough estimate. Nevertheless, we can compare this result with the simulation outcomes. Fig. 9 shows the cumulative mass profile of warm-cold gas ( $T < 10^5$  K) in the simulated MW<sup>c</sup> and M31<sup>c</sup>, that we use as a proxy for the amount of warm, ionized mass. Note that the fraction of neutral gas mass is always a very small fraction of the total amount of cold gas, and therefore we can use the cold gas safely to compare with observational results. Because observations only count gas outside the discs, we show in Fig. 9 the profiles including and excluding the galactic discs (thin and thick solid lines). In each case, to identify the galactic disc, we first rotate the galaxies to get the disc plane, and make a cylindrical cut of 30 kpc radius and 4 kpc height (more details will be presented in Section 4.3). After excluding the gaseous disc contributions, we found, for distances within 10 kpc, similar results as in observations: the MW<sup>c</sup> and M31<sup>c</sup> systems show a cold gas amount of  $M_{\text{cold}}(\leq 10 \text{ kpc}) \approx 2.1 \times 10^8 M_\odot$  and  $2.6 \times 10^8 M_\odot$  respectively. Interestingly, our cold gas mass estimates at larger scales go also in line with the results of the “COS-Halos” sample (Werk et al. 2014): a set of 38 quasar sightlines passing  $L \sim L^*$  galaxies at  $z \sim 0.2$ . On average, these authors found a lower limit of cold material of  $2 \times 10^{10} M_\odot$  within a distance of 160 kpc, whereas we

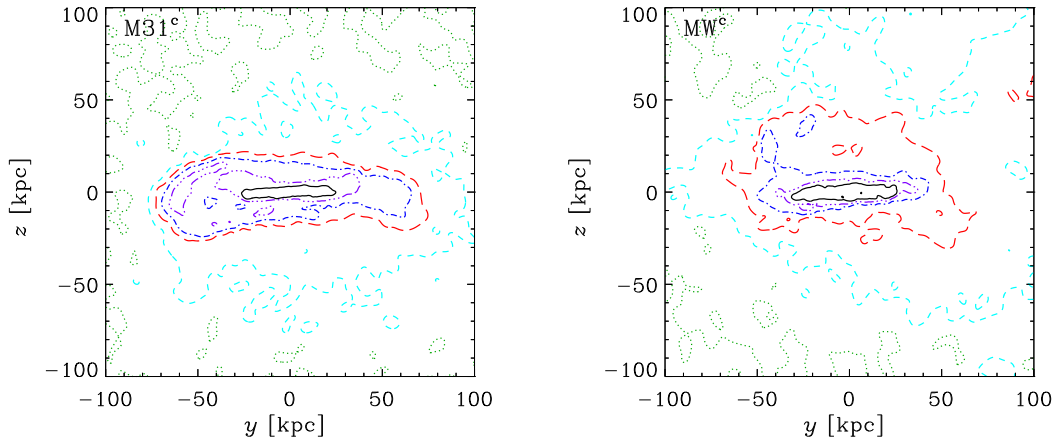


**Figure 10.** Contours of the H I gas distribution around the simulated M31<sup>c</sup> (left-hand panel) and MW<sup>c</sup> (right-hand panel) for two arbitrary edge-on views. The contours indicate column densities of  $N_{\text{HI}} \geq 10^{15} \text{ cm}^{-2}$  (dotted lines);  $N_{\text{HI}} \geq 10^{16} \text{ cm}^{-2}$  (short-dashed lines);  $N_{\text{HI}} \geq 10^{17} \text{ cm}^{-2}$  (long-dashed lines);  $N_{\text{HI}} \geq 10^{18} \text{ cm}^{-2}$  (dotted-dashed lines);  $N_{\text{HI}} \geq 10^{19} \text{ cm}^{-2}$  (three-dotted-dashed lines), and  $N_{\text{HI}} \geq 10^{20} \text{ cm}^{-2}$  (solid lines).

get a value of  $\sim 1.6 \times 10^{10} M_{\odot}$  within the virial radii of our simulated galaxies as it is shown in Table 2.

#### 4.3 H I gas component

We turn our attention to the distribution of H I gas in the simulated galaxies, and compare our results with observations. In and around the Milky Way cold gas that is predominantly neutral can be observed through radio observations of the 21 cm line if the total H I column density lies above a threshold of  $\sim 7 \times 10^{17} \text{ cm}^{-2}$  (Wakker 2004).

Gas-rich spiral galaxies such as the Milky Way and Andromeda are known to have extended H I discs with radii up to a few dozen kpc and typical H I column densities  $N_{\text{HI}} \gtrsim 10^{20} \text{ cm}^{-2}$  (e.g., Rosenberg & Schneider 2003; Zwaan et al. 2005; Levine et al. 2006, 2008). While the radial extent of the Milky Way H I disc is not possible to be measured directly owing to the interior vantage point as an observer, Braun et al. (2009) show that Andromeda has an H I disc with a radial extension of  $\sim 30$  kpc for column densities above  $N_{\text{HI}} \gtrsim 2 \times 10^{20} \text{ cm}^{-2}$  (however, see e.g. Levine et al. 2006, 2008, for a detailed analysis of the structure of the H I disc in our Galaxy).

The H I discs of our simulated M31<sup>c</sup> and MW<sup>c</sup> systems have a similar extent to those given by observations, as can be inferred from Figs. 12 and 13, where H I column density maps and covering fractions in different planes are shown (see next section for a detailed description of these figures).

Observations of the Milky Way and other nearby galaxies carried out in the 21 cm line have shown that spiral galaxies commonly also exhibit *extraplanar* H I structures that indicate inflows, outflows, and merger processes in these systems (see reviews by Wakker & van Woerden 1997; Richter 2006; Putman et al. 2012). In the Milky Way, such extraplanar neutral gas structures manifest themselves as the so-called high-velocity clouds (HVCs), which have column densities within the range  $N_{\text{HI}} \sim 10^{18} - 10^{20} \text{ cm}^{-2}$ . These are 21 cm structures observed at high galactic latitudes that

show high radial velocities that are inconsistent with a simple galactic rotation model. In Andromeda, Thilker et al. (2004) have mapped a similar population of extraplanar H I features that can be regarded as HVC analogs.

Based on 21 cm observations of the Milky Way and Andromeda galaxies, R12 developed a three-dimensional model aimed at describing the infall of extraplanar H I structures onto these galaxies, which allows to estimate the amount of neutral gas in HVCs as well as their distribution. Their modelling suggests a characteristic radial extension of  $\sim 50$  kpc for the HVCs location within galactic haloes, as well as a total H I mass in HVCs of the order of  $\sim 10^8 M_{\odot}$ .

In order to compare our simulation with the R12 model, it is necessary to exclude the H I gas in the disc region in our simulated galaxies, as we did in the previous section (we exclude particles belonging to a flat cylinder in the disc plane with a radius of 30 kpc and a height of  $\pm 2$  kpc). We note that, in our simulations, we lack the necessary resolution to resolve features like individual HVCs; however, we can use the total amount of extraplanar neutral gas as a proxy of the neutral gas mass content. The H I cumulative mass profile of our simulated galaxies including/excluding the galactic disc can be seen in Fig. 9 (thin/thick dashed lines) where we have additionally imposed two column density limits to better compare our results with observations. If no limit is applied, the resulting H I masses within 50 kpc (excluding the gaseous disc) give  $M_{\text{HI}}(r \leq 50 \text{ kpc}) \approx 3.1 \times 10^8 M_{\odot}$  and  $4.3 \times 10^8 M_{\odot}$  for the MW<sup>c</sup> and M31<sup>c</sup> galaxies respectively. In general, for higher column density limits, the mass of H I decreases by a factor of a few displaying a better match with observational mass estimates from HVCs. Additionally, the maximum spatial extent of the material with higher column density cuts tends to decrease. We checked that the precise radius assumed to exclude the discs has a negligible impact on the final neutral gas masses. For instance, for an H I disc of 40 kpc radius, the resulting mass differences are only of the order of 5%. It is worth mentioning that most of the neutral material surrounding the galaxies does not belong to



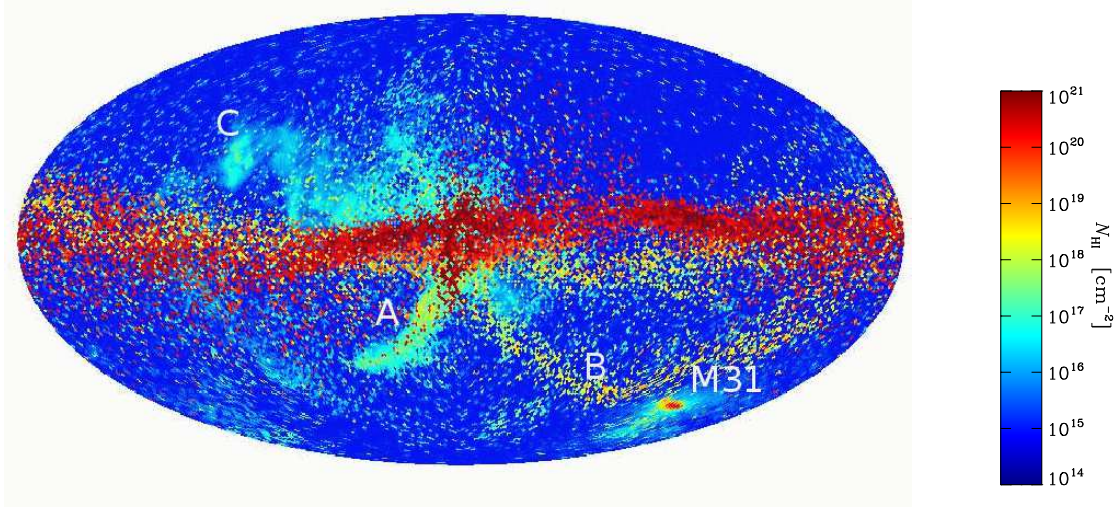


**Figure 11.** Column density of H I for the gas in our simulation with respect to the Local Standard of Rest of the MW<sup>c</sup> galaxy in a Mollweide projection (for a similar map from the H I Galactic LAB survey see Fig. 3 of Kalberla et al. 2005). The observer is located at  $(r_{\text{LSR}}, \phi_{\text{LSR}}) = (8 \text{ kpc}, 0)$  in the cylindrical coordinate system defined by the MW<sup>c</sup> disc. The M31<sup>c</sup> galaxy can be seen in the lower-right region. In addition, gaseous features labeled A, B and C are also shown (see text for details).

**Table 3.** All-sky covering fractions of H I for different column density limits, as calculated using Mollweide projections from the point of view of both MW<sup>c</sup> and M31<sup>c</sup> galaxies (Fig. 11 shows the all-sky MW<sup>c</sup> view).

$N_{\text{HI}} \text{ (cm}^{-2}\text{)}$	$> 7 \times 10^{17}$		$> 10^{16}$		$> 10^{15}$	
	M31 <sup>c</sup>	MW <sup>c</sup>	M31 <sup>c</sup>	MW <sup>c</sup>	M31 <sup>c</sup>	MW <sup>c</sup>
all gas	0.29	0.33	0.42	0.51	0.59	0.69
no disc	0.19	0.21	0.37	0.46	0.56	0.66

satellites orbiting the MW<sup>c</sup> and M31<sup>c</sup> systems. Rather, it is mainly part of the diffuse phase, and is probably associated to ambient gas. In Table 2 we present these results for all H I gas (where, essentially, most of the mass can be obtained for  $N_{\text{HI}} \geq 10^{18} \text{ cm}^{-2}$ ), as well as considering column density cuts of  $N_{\text{HI}} \geq 10^{19}$ ,  $10^{20} \text{ cm}^{-2}$ , at several relevant distances.

To characterize the properties of the neutral gas we studied its spatial location, kinematics and column density distribution. An impression of the H I distribution around the galaxies for different column densities above  $N_{\text{HI}} > 10^{15} \text{ cm}^{-2}$  is given in Fig. 10. This figure shows contour plots of the edge-on neutral gas distribution of the MW<sup>c</sup> and M31<sup>c</sup> galaxies. The solid contours represent column densities of  $N_{\text{HI}} \geq 10^{20} \text{ cm}^{-2}$ , indicating the presence of the galactic disc, while the remaining line styles stand for column densities in the range  $N_{\text{HI}} = 10^{15} - 10^{19} \text{ cm}^{-2}$  (see caption for the linestyle reference). From these plots, it can be clearly seen that most of the material with  $N_{\text{HI}} \sim 10^{18} \text{ cm}^{-2}$  is located at projected distances  $\lesssim 50 \text{ kpc}$  from the galaxy centres in accordance with observations. In particular, we found that the mean (three-dimensional) distance of the accreting neutral gas with column densities of  $N_{\text{HI}} \geq 7 \times 10^{17} \text{ cm}^{-2}$  is about 60 kpc and 70 kpc for the MW<sup>c</sup> and M31<sup>c</sup>, respectively. In general, we found that neutral material with the lowest column densities tend to be distributed in a more spherical manner than larger column density gas. This goes in line

with recent H I observations around nearby edge-on galaxies. In particular, the neutral gas contours shown in Fig. 10 are similar to those of NGC 891 as given by Oosterloo et al. (2007) (see their Fig. 1).

We have also studied the kinematics of the high column density gas complexes, finding that the mean (three-dimensional) radial velocity of the neutral gas with  $N_{\text{HI}} \geq 7 \times 10^{17} \text{ cm}^{-2}$  is of the order of  $45 \text{ km s}^{-1}$  with respect to the centre of the galaxies.

Our results are reasonably close to observational estimates; however, if no H I column density limit is applied, they show somewhat larger mass values in comparison to the R12 model. This can be explained by the fact that H I mass estimates around the Milky Way and Andromeda are mostly driven by HVC observations which represent the high-density peaks of the halo gas distribution. In fact, as can be seen in Fig. 9, after applying column density limits above those of typical HVCs, our H I mass estimates get smaller, improving the match with the R12 result. In particular, this is most noticeable in the case of our M31<sup>c</sup> simulated galaxy.

#### 4.4 Covering fractions

Among the large amount of available observational data of 21 cm line in the Milky Way, the spatial distribution of neutral gas provides an observational ground against which we can further test the results of our simulations. Such maps of the H I distribution are available for the whole sky and also in the direction of Andromeda (e.g., Braun & Thilker 2004; Braun et al. 2009). In what follows we will study the all-sky covering fractions from the point of view of our simulated MW<sup>c</sup>, as well as for the projected MW<sup>c</sup> and M31<sup>c</sup> galaxies, and compare with observations.

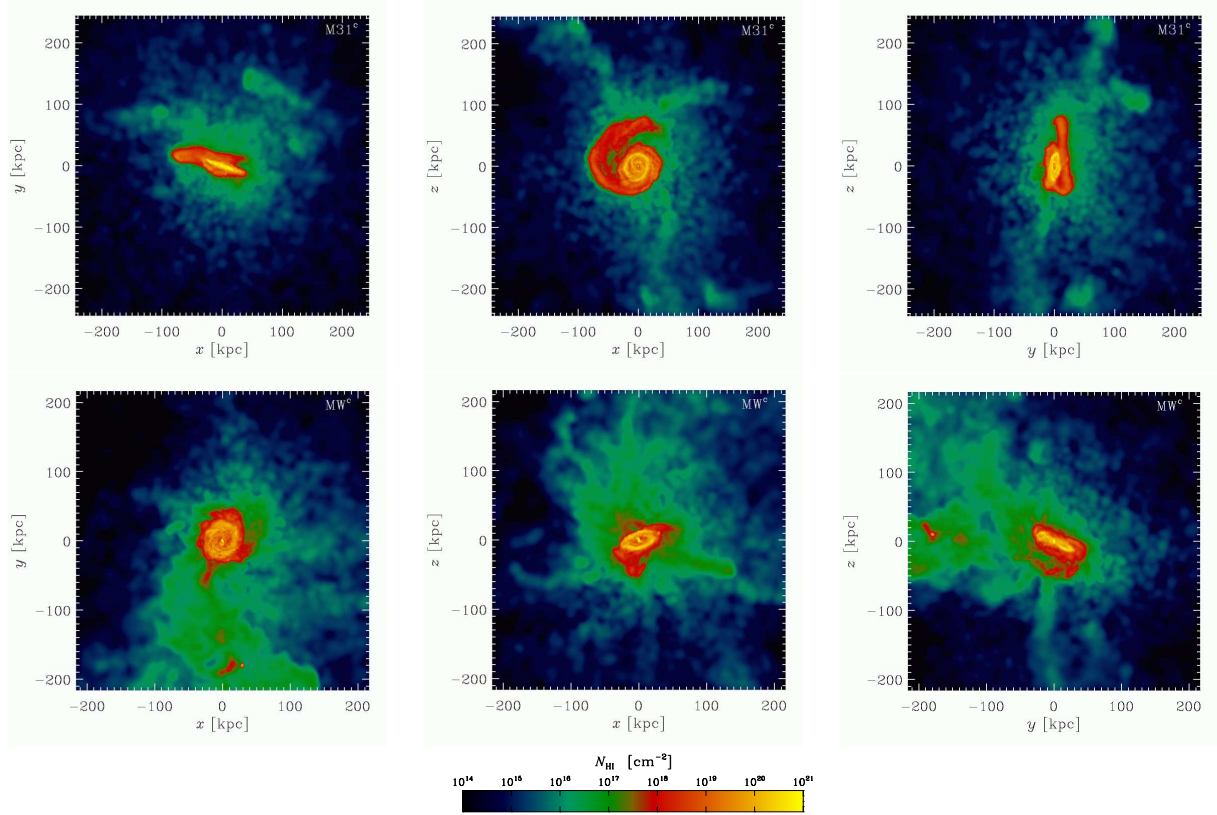


**Figure 12.** Column density of neutral hydrogen for the simulated galaxies. Upper panels: results for M31<sup>c</sup>; the left-hand panel shows the H I distribution as seen from the MW, while the middle and right ones display the remaining two perpendicular views. Lower panels: idem as the upper panels but in the case of the MW<sup>c</sup>. The plots show column densities up to the corresponding virial radius.

#### 4.4.1 All-sky map

In Fig. 11, we show an all-sky Mollweide projection of the H I column density as seen from the local standard of rest (LSR) reference system of our simulated MW<sup>c</sup>. We placed the observer at coordinates  $(r_{\text{LSR}}, \phi_{\text{LSR}})$  in the cylindrical coordinate system defined by the MW<sup>c</sup> disc, where  $r_{\text{LSR}} = 8$  kpc and  $\phi_{\text{LSR}} = 0$ . We have checked that different choices for  $\phi_{\text{LSR}}$  have no impact on the resulting all-sky map beyond the galactic disc.

In this view, the MW<sup>c</sup> disc appears as an approximately horizontal distribution of very high column density gas, with typical values of  $N_{\text{HI}} \gtrsim 10^{20} \text{ cm}^{-2}$ . The M31<sup>c</sup> galaxy is also evident as a high H I column density region ( $N_{\text{HI}} \gtrsim 10^{20} \text{ cm}^{-2}$ ) in the lower-right end of the map. A number of other interesting features are evident from this plot. A stream of cold gas, that starts close to (and within) the MW<sup>c</sup> virial radius and extends to  $\sim 400$  kpc from its centre, is responsible for the feature labelled “A”. The stream appears mainly below the disc, but also partly above it, as a result of the projection. The feature labelled “B” comes from a gas complex right outside the MW<sup>c</sup> disc, located at a distance of  $r \sim 40 - 50$  kpc. Finally, we see a  $N_{\text{HI}} \sim 10^{17} \text{ cm}^{-2}$  structure, labelled “C”, which originates well outside the MW<sup>c</sup> and M31<sup>c</sup> galaxies (at about 550 kpc from the MW<sup>c</sup> centre, in the direction opposite to M31<sup>c</sup>). For reference, we included labels “A” and “C” in our Fig. 15 and a label “B” in Fig. 7 (note that in this figure, however, the maps con-

sider all gas and not only the neutral component). While feature “B” corresponds to nearby gas, probably associated to accreting gas, both “A” and “C” structures are located at much larger distances. Therefore, our results suggest that it is possible to find neutral gas cloud complexes even outside galaxy haloes. Note, however, that some of these structures (e.g., our simulated gas cloud “C”) could be difficult to observe in emission as a result of their low column densities. Interestingly, after observing the Andromeda/M33 sky region at high-resolution, Wolfe et al. (2013) report the existence of H I material located far beyond these galaxies with column densities  $N_{\text{HI}} \gtrsim 10^{17} \text{ cm}^{-2}$  which are reminiscent of our gaseous features.

Table 3 presents the all-sky covering fraction of H I from the Mollweide projection for several column density limits:  $N_{\text{HI}} > 10^{15} \text{ cm}^{-2}$ ,  $N_{\text{HI}} > 10^{16} \text{ cm}^{-2}$ , and  $N_{\text{HI}} > 7 \times 10^{17} \text{ cm}^{-2}$ . For completeness, we also computed the all-sky covering fractions seen from M31<sup>c</sup> for an observer located at coordinates  $(r, \phi) = (8 \text{ kpc}, 0)$  as MW<sup>c</sup> and M31<sup>c</sup> show similar properties in terms of their neutral gas content. The resulting values range from about 0.3 up to 0.7 as the column density limit decreases. In particular, for  $N_{\text{HI}} > 7 \times 10^{17} \text{ cm}^{-2}$ , our results are similar to those inferred from the observations of Lockman et al. (2002) and Wakker (2004) who found  $f_c \approx 0.37$  and  $f_c \approx 0.3$  respectively. Interestingly, if we compute the all-sky covering fraction of H II, we get larger values for a given column density limit, as suggested by observations. For instance, for a threshold

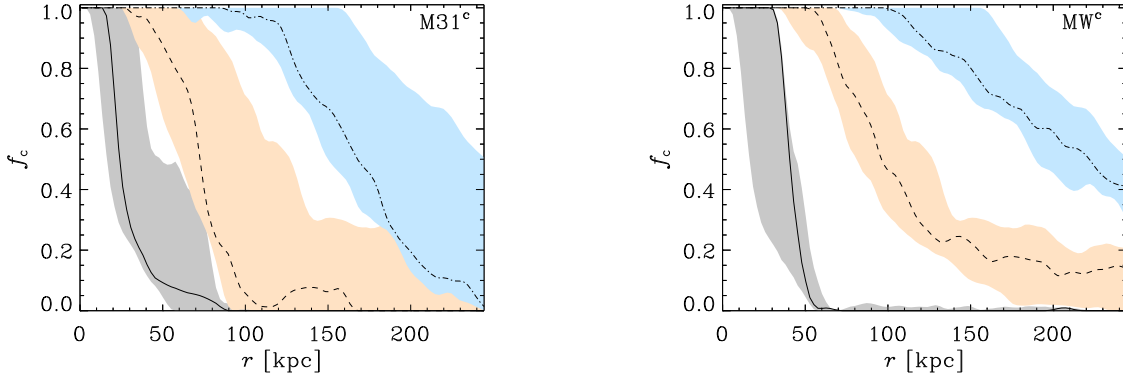


**Figure 13.** Covering fraction profile as a function of projected distance for the simulated M31<sup>c</sup> (left-hand panel) and MW<sup>c</sup> (right-hand panel) galaxies. Shown are different limits of H I column densities:  $N_{\text{HI}} > 10^{15} \text{ cm}^{-2}$  (dot-dashed lines),  $N_{\text{HI}} > 10^{16} \text{ cm}^{-2}$  (dashed lines) and  $N_{\text{HI}} > 7 \times 10^{17} \text{ cm}^{-2}$  (solid lines). The shaded areas indicate the range of possible covering fraction values after choosing different viewing angles.

of  $N_{\text{HI}} \gtrsim 3 \times 10^{19} \text{ cm}^{-2}$  we get an all-sky covering fraction of 0.86. In comparison, Shull et al. (2009) estimated a Milky Way value of  $f_c = 0.81$  for  $N_{\text{HI}} \gtrsim 6 \times 10^{18} \text{ cm}^{-2}$ . In this respect, to improve the agreement between our model and observations, we would need to increase the spatial resolution of our simulation, as well as to include relevant physical processes at smaller scales (e.g., radiative transfer effects).

#### 4.4.2 Projected galaxy fields

In order to further investigate the H I column densities in a way that is comparable to actual zoomed-in field views, we show in the left-hand panels of Fig. 12 the distribution of H I column density for M31<sup>c</sup> as seen from the MW<sup>c</sup> (upper panel) and for the MW<sup>c</sup> as seen from M31<sup>c</sup> (lower panel). These maps allow us to estimate H I projected covering fractions, which is a useful quantity to compare to observational results. From our plots, it is clear that, when we see M31<sup>c</sup> from the MW, it appears more or less edge-on; in contrast, the MW, as seen from M31<sup>c</sup>, appears almost face-on. This difference will strongly affect estimations of covering fractions, in particular for high column densities, e.g.  $N_{\text{HI}} > 7 \times 10^{17} \text{ cm}^{-2}$ , since the disc regions (which are the dominant H I component) always fulfill this condition and the area covered by the disc strongly depends on the viewing angle.

In Fig. 13 we show, for M31<sup>c</sup> (left-hand panel) and MW (right-hand panel), the radial profiles of the covering fraction up to the virial radius of each galaxy for three H I column density limits; i.e.,  $N_{\text{HI}} > 10^{15} \text{ cm}^{-2}$  (dot-dashed lines);  $N_{\text{HI}} > 10^{16} \text{ cm}^{-2}$  (dashed lines), and  $N_{\text{HI}} > 7 \times 10^{17} \text{ cm}^{-2}$  (solid lines). We found that, when the limit  $N_{\text{HI}} > 7 \times 10^{17} \text{ cm}^{-2}$  is considered, the covering fractions  $f_c$  decrease quickly with radius as we go outside the disc region:  $f_c$  goes from 1 to values close to zero at  $r \approx 90 \text{ kpc}$  for M31<sup>c</sup> and  $r \approx 60 \text{ kpc}$  for the MW<sup>c</sup>. If we take reference values at  $r = 30 \text{ kpc}$  and  $r = 50 \text{ kpc}$ , we found that  $f_c(r = 30 \text{ kpc}) \approx 0.3$  and  $f_c(r = 50 \text{ kpc}) \approx 0.1$  for M31<sup>c</sup>, and that  $f_c(r = 30 \text{ kpc}) \approx 1$  and  $f_c(r = 50 \text{ kpc}) \approx 0.1$  for MW<sup>c</sup>. The fact that the covering fraction at 30 kpc is close to 1

and 0.3 for the MW<sup>c</sup> and M31<sup>c</sup>, respectively, can be understood in terms of the projections shown in Fig. 12: the MW<sup>c</sup> appears almost face-on and, therefore, displays very high covering fractions up to larger radii, only decreasing near the disc edge; whereas M31<sup>c</sup> appears almost edge-on, thus decreasing the covering fraction for smaller radii. Our results, in particular those for M31<sup>c</sup>, show a similar trend to the estimates of R12 who determined covering fractions of  $f_c(r = 30 \text{ kpc}) \approx 0.15$  and  $f_c(r = 50 \text{ kpc}) \approx 0.05$  for Andromeda.

In our simulation, the relative position between the galactic discs turned out to be almost perpendicular. However, the simulation gives us the possibility to construct mock H I observations for each galaxy to “observe” them in any possible viewing angle. For example, in the middle- and right-hand panels of Fig. 12 we show the results for two additional projections, i.e., perpendicular to those shown in the corresponding left-hand panels. From this plot it is clear that the covering fractions vary significantly when seeing the galaxies in different projections showing that this effect will be certainly important in any observational estimation of H I covering fractions.

To quantitatively test the effect of different viewing angles on the covering fractions, we “observe” each simulated galaxy from different locations. The shaded areas in Fig. 13 show the range of all possible covering fraction values as a result of the varying viewing angle. As expected, we found that the M31<sup>c</sup> covering fractions, as seen from the MW, are close to the minimum possible values since M31<sup>c</sup> is almost edge-on in this view. In contrast, as seen from M31<sup>c</sup>, the simulated MW<sup>c</sup> is close to face-on and, consequently, displays a covering fraction that is similar to the maximum possible values.

Fig. 13 also shows the covering fractions (as well as the corresponding shaded areas; see above) for two other H I column density limits, namely,  $N_{\text{HI}} > 10^{16} \text{ cm}^{-2}$  and  $N_{\text{HI}} > 10^{15} \text{ cm}^{-2}$ . As expected, in these cases, the covering fractions remain at  $f_c \approx 1$  up to much larger radii. In the case of M31<sup>c</sup>, the covering fraction for  $N_{\text{HI}} > 10^{15} \text{ cm}^{-2}$  decreases significantly, being close to zero at the virial radius.



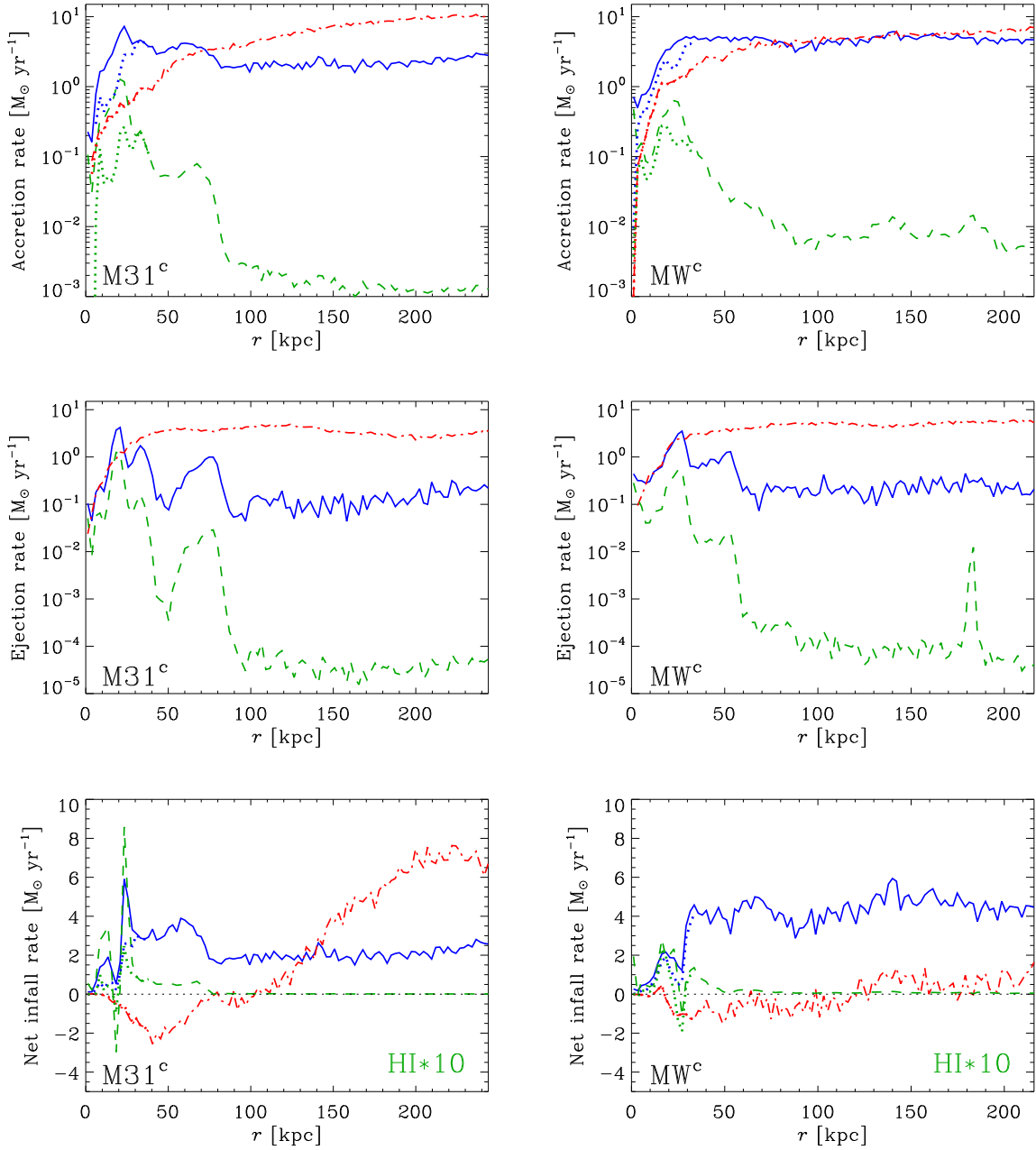


**Figure 14.** Accretion, ejection and net infall rate profiles (spherically-averaged; upper, middle and lower panels, respectively) for gas belonging to the M31<sup>c</sup> (left-hand panels) and MW<sup>c</sup> (right-hand panels) simulated galaxies. Different gas components are shown: hot (dot-dashed lines), cold (solid lines) and HI (dashed lines). For the accretion case, we also include rates excluding the gaseous discs (dotted lines, as explained in Section 4.3). Note that the latter is only relevant for  $r \lesssim 30$  kpc. Also note that the net infall rate of HI has been multiplied by 10 to allow a proper visualization.

In contrast, for the MW<sup>c</sup>, the covering fraction is  $f_c \approx 0.4$  even at the virial radius, indicating that the gas distribution extends beyond it. A similar behaviour is seen for the resulting covering fractions when a column density limit of  $N_{\text{HI}} > 10^{16} \text{ cm}^{-2}$  is adopted. A notable bump at  $r \sim 150$  kpc demonstrates that the covering fraction can be non-zero for any radius, as long as there are clumps of neutral gas and/or infalling neutral material and their associated tidal gas features within the halo.

## 5 ACCRETED AND EJECTED GAS

In this section, we study the accretion and ejection rates for the simulated MW<sup>c</sup> and M31<sup>c</sup> galaxies, and compare our results with recent estimates from observational data.

We calculate the gas accretion/ejection rates at  $z = 0$  by considering the velocity of gas particles lying at a spherical surface located at a given distance from the centre of the simulated galaxies and up to the corresponding virial

**Table 4.** Integrated accretion and ejection rates of the simulated MW<sup>c</sup> and M31<sup>c</sup> galaxies for the cold, hot and H I gas phases within a distance of  $r = 10$  kpc and  $r = 50$  kpc from the corresponding galactic centres. The inflow/outflow characteristic time of the different components has been obtained by dividing the gas distance to its radial velocity (see Section 5.4). Quantities including the gaseous galactic discs are shown within brackets; as expected, the hot component is the less one affected by the disc exclusion. For  $r \leq 50$  kpc, we also show results for the accretion rates, excluding the gaseous discs, for column density limits of  $N_{\text{HI}} > 10^{18}$ ,  $10^{19}$  and  $10^{20} \text{ cm}^{-2}$ .

Rate ( $M_{\odot} \text{ yr}^{-1}$ )	Accretion		Ejection	
	M31 <sup>c</sup>	MW <sup>c</sup>	M31 <sup>c</sup>	MW <sup>c</sup>
$\dot{M}(r \leq 10 \text{ kpc})$ :				
Hot	0.16 (0.21)	0.09 (0.19)	0.11 (0.23)	0.17 (0.25)
Cold	0.33 (1.68)	0.57 (2.38)	0.05 (0.59)	0.35 (1.26)
H I	0.04 (0.62)	0.11 (1.12)	0.01 (0.28)	0.10 (0.66)
$\dot{M}(r \leq 50 \text{ kpc})$ :				
Hot	1.18 (1.25)	2.14 (2.40)	2.59 (2.82)	3.03 (3.31)
Cold	3.75 (7.80)	5.10 (8.11)	0.75 (2.64)	1.51 (3.08)
H I	0.22 (1.40)	0.34 (1.54)	0.09 (0.77)	0.23 (0.90)
H I ( $N_{\text{HI}} > 10^{18} \text{ cm}^{-2}$ )	0.21	0.33	–	–
H I ( $N_{\text{HI}} > 10^{19} \text{ cm}^{-2}$ )	0.16	0.28	–	–
H I ( $N_{\text{HI}} > 10^{20} \text{ cm}^{-2}$ )	0.06	0.15	–	–

radius. We estimate the amount of accretion (ejection) of gas using particles that are infalling (outflowing) near this boundary taking into account the time it would take them to cross it inwards (outwards). We do this for all gas, but also separately for the hot, cold and H I gas components.

Fig. 14 shows the accretion, ejection and net infall rates for M31<sup>c</sup> (left-hand panels) and MW<sup>c</sup> (right-hand panels) in the case of cold, hot, and H I gas. For accretion and net infall rates we also show results for the cold and H I phases excluding (dotted lines) and including (otherwise) the gaseous disc region in each case (as explained in Section 4.3). In this way, we can discriminate infalling material associated to the disc from that belonging to the gaseous galactic halo which is the one we are mainly interested in. However, as expected, differences between these two measures are only appreciable at distances smaller than  $\sim 30$  kpc, i.e. close to the radius of the removed disc region. In what follows, for such small scales, we will always refer to estimates *excluding* the gaseous discs.

### 5.1 Accretion rate profiles

The accretion rate profiles of our simulated galaxies are shown in Fig. 14 (upper panels). We found that the accretion rates at distances  $r \gtrsim 70$  kpc are dominated by hot gas, reaching values of  $7 - 10 M_{\odot} \text{ yr}^{-1}$  near the virial radius, where the cold mode accretion has typical values of  $3 - 5 M_{\odot} \text{ yr}^{-1}$ . At smaller distances, the main contribution is, conversely, owing to the cold gas component, with typical rates of a few  $M_{\odot} \text{ yr}^{-1}$ , followed by the hot and H I accretion modes respectively. The transition between the dominance of the hot and cold modes is directly connected to the cooling efficiency as this quantity – and therefore the accretion rate – is higher for gas in the central regions than for material located in the haloes, which are at temperatures close to  $10^6$  K (see Figs. 5 and 8).

The H I accretion rates reach a peak of  $\sim 0.25 M_{\odot} \text{ yr}^{-1}$  at 20 kpc, and decrease significantly at larger radii, reaching very small values of  $\sim 10^{-3} - 10^{-2} M_{\odot} \text{ yr}^{-1}$  as one approaches the virial radius. Interestingly, in the case of M31<sup>c</sup>, most of the H I accretion comes from gas located within a

distance of  $\sim 50 - 70$  kpc, in agreement with HVC data, as well as with the modelling of R12.

### 5.2 Ejection rate profiles

The ejection rate profiles can be seen in the middle panels of Fig. 14 (note the different  $y$ -scale). As expected, most of the ejected gas corresponds to the hot phase which is intimately related to the process of supernova feedback. The presence of outflowing material is a direct consequence of the mass-loaded galactic winds. In our model, such winds are naturally generated after supernova explosions, in some cases being able to reach the virial radius and penetrate in the intergalactic medium (see e.g., Scannapieco et al. 2006). The winds are particularly evident at distances  $r \gtrsim 50$  kpc (i.e., greater than the size of the galactic discs) with typical hot gas ejection rates of the order of  $\sim 5 M_{\odot} \text{ yr}^{-1}$ .

The ejection rates of cold and neutral material at distances larger than  $\sim 50$  kpc are smaller compared to those of the hot phase:  $\sim 0.1 M_{\odot} \text{ yr}^{-1}$  and  $\sim 5 \times 10^{-5} M_{\odot} \text{ yr}^{-1}$ , respectively. At  $r \lesssim 50$  kpc, we find higher ejection rates, although these are still relatively low, particularly in the case of H I material. As shown in Figs. 4 and 7, the gas distributions in the inner regions of galaxies are extremely complex owing to the interplay between cooling, heating and accretion. Outflowing cold/H I gas is the result of a pressure support gain, either directly via energy feedback (even if they cool out rapidly afterwards) or via the local hot phase.

### 5.3 Net infall rate profiles

The net infall of gas for our two simulated galaxies can be calculated, as a function of radius, as the difference between the corresponding accretion and ejection rate profiles. These can be seen in the lower panels of Fig. 14, where, for clarity, we have multiplied the net infall of neutral gas by 10. The results indicate that there is a net infall of cold gas of  $\sim 2 - 5 M_{\odot} \text{ yr}^{-1}$  at distances greater than  $\sim 30$  kpc, whereas the neutral (H I) material accumulates onto the galaxies at a rate of  $\sim 0.05 - 0.1 M_{\odot} \text{ yr}^{-1}$  for distances smaller than  $r \sim 70$  kpc,

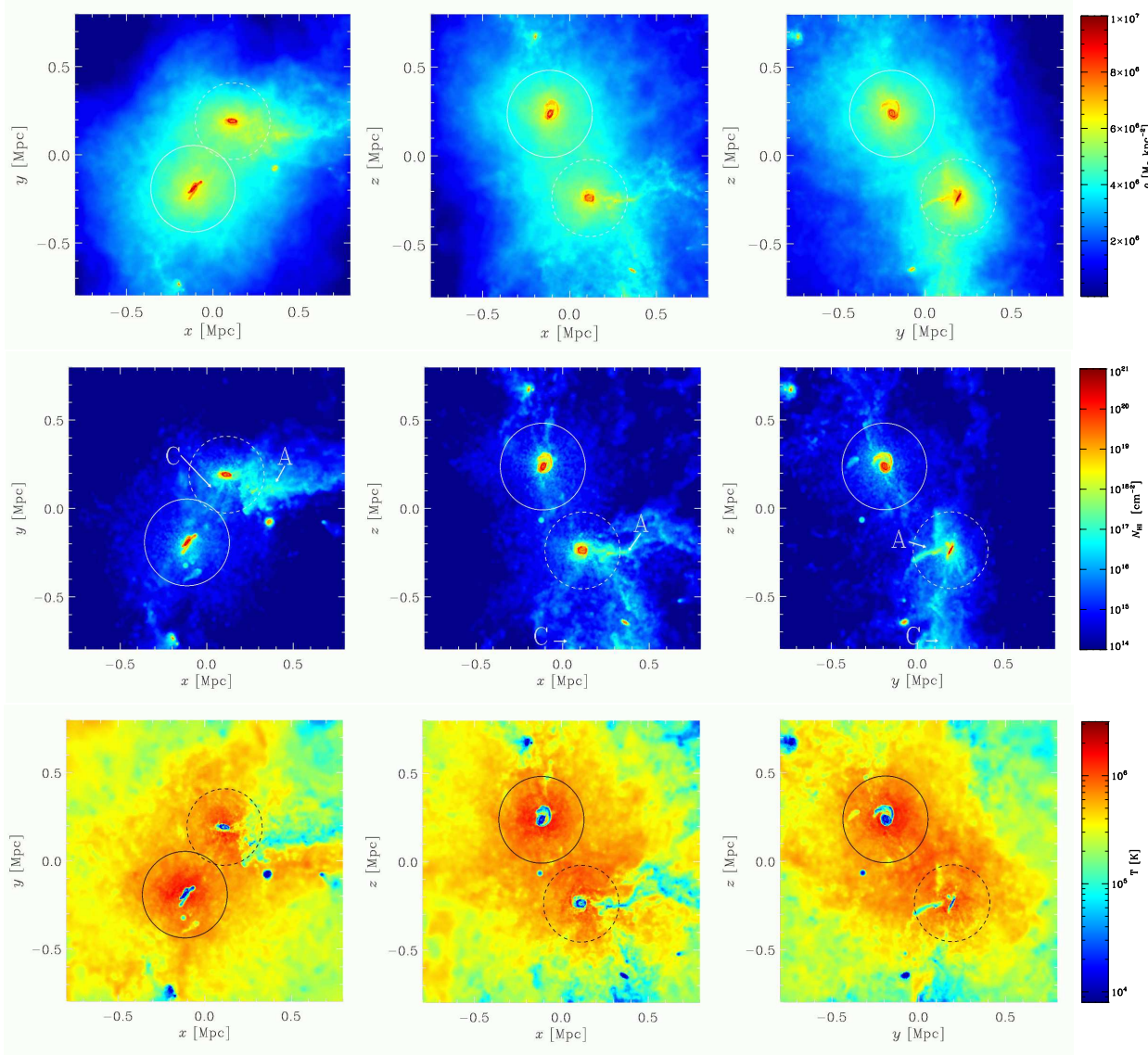


**Figure 15.** Gas density (upper panels), H I column density (middle panels) and temperature (lower panels) maps for the M31<sup>c</sup>/MW<sup>c</sup> system. Each row shows three perpendicular projections of the corresponding quantity, in order to highlight the three-dimensional distributions. The virial radii of M31<sup>c</sup> and the MW<sup>c</sup> are indicated by the solid and dashed circles, respectively. Prominent neutral gas features are indicated (see text).

as indicated by the corresponding dotted lines (see caption of Fig. 14).

In the case of hot gas, our simulated galaxies show a clear transition scale, located at about 100 – 120 kpc from the galactic centres, below (above) which hot gas is being ejected (accreted). This is an indication of the strength of the supernova-driven winds, which weaken with increasing radius. The precise values of the net infall rates depend on the particular galaxy considered. For instance, in the case of M31<sup>c</sup>, we found a net accretion (ejection) of hot gas  $\lesssim 7 M_{\odot} \text{ yr}^{-1}$  ( $\lesssim 2 M_{\odot} \text{ yr}^{-1}$ ) above (below) the transition scale, whereas, for the MW<sup>c</sup>, the resulting net rates (both of accretion and ejection) are more modest, namely,  $\lesssim 1 M_{\odot} \text{ yr}^{-1}$  (see dot-dashed lines in the bottom panels of Fig. 14). The net accretion rates of *all* material (neutral+cold+hot) at the virial radius of the galaxies are about 6 – 8  $M_{\odot} \text{ yr}^{-1}$ .

In the next section we compare our predictions for the accretion rates of cold and neutral material with observations. Unfortunately, there are no available observational estimates on the hot gas accretion, as well as on the ejection rates, but, in relation to the latter, our results above indicate that outflowing material might be present near the virial radius of galaxy-sized haloes, although at low densities.

## 5.4 Cold and H I gas accretion rates

### 5.4.1 Comparison with observations

Observational estimates of the gas accretion rates onto the Milky Way galaxy are done using the cold and neutral gas components. In this section, we compare the accretion rates of our simulated galaxies with such observations. Table 4



shows the *integrated* accretion/ejection rates of the simulated M31<sup>c</sup> and MW<sup>c</sup> for the cold and neutral gas phases (we also show results for the hot phase, for completeness). To resemble observational methodologies we compute, in each case, the characteristic inflow (outflow) time by dividing the distance of the gas clouds to the centre of the galaxy to their corresponding radial velocities. Results are shown for two scales of interest, including all material within a distance of  $r = 10$  kpc and  $r = 50$  kpc, and excluding the gaseous discs (as explained in Section 4.3), to meaningfully compare with observational results. This means that material within the boundaries of our gaseous discs will not contribute to our mass infall estimates. In particular, when considering scales  $r \leq 10$  kpc, only material above and below the discs will be considered as a result of this approach.

As mentioned in Section 4.2, the mass of cold gas in the Milky Way halo at a distance of  $\sim 10$  kpc above the galactic plane has been estimated in  $\sim 10^8 M_\odot$ . If this gas would represent infalling material, its contribution to the gas-accretion rate of the Milky Way would be, as a first approximation, of the order of  $\sim 1 M_\odot \text{ yr}^{-1}$  (Shull et al. 2009; Lehner & Howk 2011). In our simulation, the *integrated* accretion rates of cold gas within 10 kpc (excluding the gaseous disc) are  $0.33 M_\odot \text{ yr}^{-1}$  and  $0.57 M_\odot \text{ yr}^{-1}$  for M31<sup>c</sup> and MW<sup>c</sup>, respectively. Interestingly, the resulting MW<sup>c</sup> value is of the same order of magnitude than in observations. If the discs were not excluded, the rates for both galaxies would result a factor of  $\sim 4 - 5$  larger, as it is shown in Table 4.

Observational estimates for the infall of neutral gas in the form of HVCs in the Milky Way are within the range  $\sim 0.1 - 0.5 M_\odot \text{ yr}^{-1}$  when integrating the contributions of all known H I gas complexes (e.g., Wakker 2004; Wakker et al. 2007, 2008; Putman et al. 2012). The three-dimensional modelling of R12 gives, instead, an accretion rate of  $\sim 0.7 M_\odot \text{ yr}^{-1}$  inside a spherical region of  $\sim 50$  kpc radius. In the case of neutral material in our simulations, we found that the accretion rates of *all* H I gas within this distance are  $\dot{M}_{\text{HI}}(r \leq 50 \text{ kpc}) \approx 0.22 M_\odot \text{ yr}^{-1}$  and  $0.34 M_\odot \text{ yr}^{-1}$  for M31<sup>c</sup> and MW<sup>c</sup>, respectively, i.e. consistent with the range of observed accretion rate values for the Milky Way but a factor 2 – 3 smaller than the R12 modelling. When repeating the same calculation but imposing column density cuts to the accreting material we obtain similar results: H I gas with projected densities of  $N_{\text{HI}} \geq 10^{18}, 10^{19}, 10^{20} \text{ cm}^{-2}$  displays accretion rates of  $\dot{M}_{\text{HI}}(r \leq 50 \text{ kpc}) \approx 0.21, 0.16, 0.06 M_\odot \text{ yr}^{-1}$  and  $0.33, 0.28, 0.15 M_\odot \text{ yr}^{-1}$  for the M31<sup>c</sup> and MW<sup>c</sup> simulated galaxies, respectively. For column density cuts corresponding to HVCs with  $N_{\text{HI}} \geq 10^{19} \text{ cm}^{-2}$  the *integrated* H I accretion rates decrease by less than 30%, still remaining consistent with observations. For the largest column density values the rates show a significant decrease. This could indicate the need for a higher spatial resolution in our simulation to better describe the most compact gas complexes.

#### 5.4.2 Comparison with star formation rate

At this point, it is interesting to compare the accretion rate of gas onto the simulated galaxies with their star formation rate (SFR) as accreting material is believed to be responsible of sustaining the star formation activity. As mentioned before the integrated accretion rate of neutral gas within

50 kpc is about  $0.2 - 0.3 M_\odot \text{ yr}^{-1}$  (see Table 4), which is consistent to the local rate estimates obtained at the termination of the discs. These values are smaller than the typical SFRs of our simulated galaxies at  $z = 0$ , which are about  $1 M_\odot \text{ yr}^{-1}$  (see Scannapieco et al. 2014). However, as stated before, most of the accreting cold gas is not in the neutral phase, thus providing more fuel that can eventually be transformed into stars. In fact, as can be seen in Table 4, typical cold gas accretion rates within a 50 kpc region are about  $4 - 5 M_\odot \text{ yr}^{-1}$ , although only a fraction of it may undergo star formation. This suggests that, in this way, it could be possible to maintain the continuous star formation rate required in observed present-day galaxies.

## 6 GAS DISTRIBUTION IN THE SIMULATED MILKY WAY/ANDROMEDA SYSTEM

We turn our focus to the study of the gas distribution in the MW<sup>c</sup>/M31<sup>c</sup> system and, in particular, in the region between the two galaxies. The main question we want to address is whether there is a gas excess between M31<sup>c</sup> and MW<sup>c</sup>, in relation to the amount of gas in any other random direction.

Fig. 15 shows maps of total gas density, H I column density and temperature for the MW<sup>c</sup>/M31<sup>c</sup> system, at  $z = 0$ , in a cubic box of 1.6 Mpc on a side. The origin is located in the geometric centre of the two galaxies, and the circles show the virial radii of M31<sup>c</sup> (solid lines) and MW<sup>c</sup> (dashed lines). Clearly, the gas distribution of the two haloes overlap suggesting that the gaseous haloes are interconnected, and the presence of a gas bridge in that particular direction. Interestingly, some of the neutral gas clouds between the galaxies have column densities of  $N_{\text{HI}} \sim 10^{17} \text{ cm}^{-2}$  (middle panels), thus resembling those observed by Wolfe et al. (2013) in the direction linking Andromeda and M33 galaxies. The temperature maps also show that there is no clear separation of the gas in the two galaxies, neither there is significant temperature difference between the two haloes (see also Section 3).

To further investigate this, we plot in Fig. 16 the Hydrogen number density profile as a function of radius, after centring our reference system in the MW<sup>c</sup> galaxy. The plot is done up to a distance of 652 kpc, where the M31<sup>c</sup> galaxy is located. We first constructed the density profiles, from the MW<sup>c</sup> centre, along random line-of-sights, and we plotted the mean over these profiles (dashed line), as well as the corresponding  $\pm 1\sigma$  regions (shaded region). For comparison, the mean cosmological number density of Hydrogen is shown as a horizontal dotted line. Interestingly, for distances smaller than  $\sim 100$  kpc, our simulated density values are consistent, within a  $1\sigma$  deviation, to the average *electron* number density limits derived by several authors (Bregman & Lloyd-Davies 2007; Grcevich & Putman 2009; Gupta et al. 2012; Miller & Bregman 2013, see Fig. 16). For distances close to the virial radius of the MW<sup>c</sup>, our simulation gives a similar result to that inferred by Blitz & Robishaw (2000), which estimate an electron number density of  $n_e \approx 2.4 \times 10^{-5} \text{ cm}^{-3}$  within a distance of  $\sim 250$  kpc from the Sun by studying the depletion of cold gas in dwarf spheroidal galaxies as a result of ram pressure stripping. We note, however, that this comparison must be

taken with caution as the Blitz & Robishaw (2000) estimation is not free of uncertainties.

The thick black line in Fig. 16 shows the Hydrogen number density profile corresponding to the line-of-sight towards M31<sup>c</sup>. We found a clear gas excess in this direction: the Hydrogen number density between the two galaxies is about  $n_{\text{H}} \sim 4 \times 10^{-5} \text{ cm}^{-3}$ , which is well above the gas density at this distance for a random line-of-sight (i.e., about  $10^{-5} \text{ cm}^{-3}$ ; see dashed line). If we consider the spread of the random sightline values the significance of the gas excess detection at a distance of  $\sim 300 \text{ kpc}$  from the MW<sup>c</sup> is close to  $20\sigma$ . As we further approach to the simulated M31<sup>c</sup>, the gas density profile rapidly increases owing to the presence of the M31<sup>c</sup> gaseous halo, while for any other random direction the mean number density profile slightly decreases approaching to the mean cosmological value.

A gas bridge between the Milky Way and Andromeda may be supported by observations of high-velocity O VI absorption in the Far-UV. Sembach et al. (2003) and Wakker et al. (2003) (as shown by their Figs. 10–12) found an excess of relatively strong O VI absorption with high negative radial velocities ( $v_{\text{LSR}} \approx -400$  to  $-150 \text{ km s}^{-1}$ ) at  $l \approx 20^\circ - 140^\circ$  and  $b \lesssim 30^\circ$ , i.e. including the position of Andromeda. A possible scenario explaining these observations could be a general excess of hot gas towards this region, as implied by our simulation. In such a case, the observed O VI absorption features may indicate somewhat cooler gas patches at  $T \sim 3 \times 10^5 \text{ K}$  that condense out of the ambient hot ( $T \sim 10^6 \text{ K}$ ) medium which comprises the bulk of the gas that interconnects the Milky Way and Andromeda galaxies (see Fig. 15).

However, it is worth noting that the interpretation of the Sembach et al. (2003) and Wakker et al. (2003) observations is not straightforward, as O VI absorption at high negative radial velocities is ubiquitous at  $l < 180^\circ$ , a sky region also occupied by many prominent 21 cm HVCs with  $v_{\text{LSR}} < 100 \text{ km s}^{-1}$  (e.g., the Magellanic Stream and Complexes A, C, H; see Fig. 1 in Richter et al. 2009). Therefore, the observed O VI absorption could also be produced by the existence of transition-temperature gas in an extended boundary between the neutral body of the mentioned halo clouds and the surrounding hot halo gas.

After repeating the exercise presented in Fig. 16 for different redshifts we discovered that the gas excess is first seen in the simulation at  $z \sim 1$  as a result of the kinematical evolution of the LG, when the two haloes overlap and are part of the same filament. However, a detailed analysis of the gas distribution as a function of redshift will be presented in a forthcoming work.

## 7 COMPARISON WITH RECENT WORK

In this section, we compare our results with the work of Fernández et al. (2012) and Joung et al. (2012) (hereafter F12 and J12, respectively). These authors studied the neutral and ionized gas components of a galaxy with a halo mass of  $1.4 \times 10^{12} M_\odot$  that formed in a cosmological simulation, run with the Adaptive Mesh Refinement code ENZO. In general, our results are in reasonable agreement with those of F12 and J12, as we explain below. Note, however, that variance in the galaxy properties are expected, even for a given

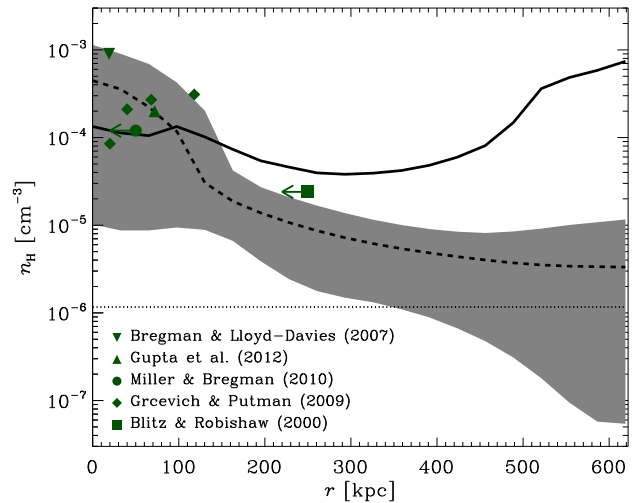


**Figure 16.** Hydrogen number density profile as function of distance to the MW<sup>c</sup> mass centre for different random directions. The mean value is indicated as a dashed line, while the shaded region corresponds to the standard deviation. The thick black line corresponds to the direction towards the M31<sup>c</sup> galaxy. For comparison, we show the cosmological Hydrogen number density as a dotted line. Filled symbols indicate estimates of the observed *electron* number density at different distances from the Milky Way which have been included as reference values. Arrows indicate an upper limit for the corresponding path-length.

halo mass. Therefore, disagreement can only be established when differences are larger than the expected scatter that naturally arises in hierarchical galaxy formation models<sup>3</sup>.

We first compare the total H I masses, excluding the gaseous disc and within the inner 50 kpc, as to be consistent with the outcomes of F12. These authors found a lower H I mass of about  $10^8 M_\odot$ , when compared to our results, for which we found H I masses of  $3 - 4 \times 10^8 M_\odot$ . Overall, the resulting mass profiles are similar, although in F12 there is a larger number of peaks, presumably owing to their better spatial resolution. The gaseous halo of F12 agrees well with ours in terms of their typical temperature, which is always of the order of  $10^6 \text{ K}$ . The most significant difference between F12 and our work is on the size of the gaseous neutral discs. In F12, they found a typical radial extension of about 15–20 kpc, significantly smaller than the 30–40 kpc we found for our galaxies. In this respect, our results are in better agreement with observations, and allow the formation of more extended stellar discs, as shown in Scannapieco et al. (2014).

Concerning the accretion rates given in F12, they quoted an H I accretion rate onto the disc of  $\sim 0.2 M_\odot \text{ yr}^{-1}$ , at a radius of 20 kpc and excluding the disc. If we do the same calculation, we find a similar value of  $\sim 0.25 M_\odot \text{ yr}^{-1}$  for our simulated galaxies (see the dotted lines in the top panels of Fig. 14). If we take, instead, a radius of 30 kpc,

<sup>3</sup> It is worth noting also that, ultimately, an unbiased comparison between the two sets of simulations is not entirely possible owing to the different hydrodynamical and star formation/feedback implementations adopted in each case.

which is closer to the size of our simulated discs, we obtain smaller accretion rates of  $\sim 0.1 - 0.2 \text{ M}_\odot \text{ yr}^{-1}$ .

J12 focused on the net infall rates of the different gas phases, excluding always the gas disc in their analysis and adopting a similar criterium than ours (nevertheless, note that the disc exclusion region is different, as a result of its smaller size). Our simulation shows that the gas inflow at distances larger than the disc sizes are dominated by ionized material belonging both to the cold ( $T < 10^5 \text{ K}$ ) and hot ( $T > 10^5 \text{ K}$ ) gas phases, in line with the findings of J12. We find, however, a significant discrepancy in the net accretion rates for the hot phase (which corresponds to that of “warm-hot” and “hot” phases of J12) in the inner regions (i.e.,  $r \lesssim 50 - 100 \text{ kpc}$ ): whereas we get a net *ejection* rate of about  $1 - 2 \text{ M}_\odot \text{ yr}^{-1}$ , J12 find a net *accretion* rate of about  $1 - 3 \text{ M}_\odot \text{ yr}^{-1}$ . This indicates that the implementation of the feedback mechanism in the two simulations works differently. Our model is much more efficient in driving supernova outflows, which is also the reason for getting more extended gaseous/stellar discs. At larger distances, i.e.  $r \gtrsim 100 \text{ kpc}$ , the net accretion rates between the simulations are more similar: we find rates within the range  $\sim 1 - 6 \text{ M}_\odot \text{ yr}^{-1}$  compared to the  $\sim 1 - 5 \text{ M}_\odot \text{ yr}^{-1}$  obtained by J12. For the cold phase, the net accretion rates of our simulated galaxies are within the range  $\sim 2 - 5 \text{ M}_\odot \text{ yr}^{-1}$  in comparison with  $\sim 0.5 - 2 \text{ M}_\odot \text{ yr}^{-1}$  in the J12 case. Note that our simulation, having two galaxies of a similar mass, gives an estimate of the (minimum) variations expected from halo-to-halo, and, therefore, agreement must be gauged taking this into account.

## 8 SUMMARY AND CONCLUSIONS

We have studied the gas distribution within and between the two largest members of a simulated Local Group of galaxies using a constrained cosmological simulation. The two simulated galaxies, dubbed MW<sup>c</sup> and M31<sup>c</sup>, approximately resemble the real Milky Way and Andromeda galaxies in terms of their masses, separation, inclination and relative velocity and are surrounded by a large-scale environment similar to the one observed in the real LG. The numerical experiment was carried out using the simulation code GADGET3 with the extensions of Scannapieco et al. (2005, 2006) that include a multiphase gas model, a treatment of supernova (thermal) feedback, chemical enrichment and metal-dependent cooling.

We studied the main properties (e.g., masses, distribution, accretion/ejection rates, covering fractions) of the gaseous material belonging to our simulated galaxies for different gas phases (i.e., hot:  $T \geq 10^5 \text{ K}$ ; cold:  $T < 10^5 \text{ K}$ , and H I neutral gas) and compared our results with available observations.

The main results of our work can be summarized as follows:

- The gas distribution within the simulated MW<sup>c</sup> and M31<sup>c</sup> haloes is characterized by the presence of a dense ( $\rho \gtrsim 5 \times 10^4 \text{ M}_\odot \text{ kpc}^{-3}$ ) region with  $T \sim 10^4 \text{ K}$  located in the central parts ( $r \lesssim 30 \text{ kpc}$ ) plus an additional gaseous halo component (which for our analysis we divide into two phases according to a temperature criterium). Generally speaking, within the halo, the cold gas phase dominates

over the hot one for  $r \lesssim 50 \text{ kpc}$ , while the opposite is true at larger scales. The mean temperature of the simulated gaseous coronae at the virial radius is about  $7 \times 10^5 \text{ K}$ . This value is close to the estimate given by Gupta et al. (2012) for the warm-hot material surrounding the Milky Way inferred through O VII absorption lines. The amount of hot gas within the virial radii of our simulated MW<sup>c</sup> and M31<sup>c</sup> galaxies is of the order of  $\sim 5 \times 10^{10} \text{ M}_\odot$ . Interestingly, this value is also consistent with the findings of Gupta et al. (2012). Under plausible assumptions, these authors claim the existence of a large hot gas reservoir of mass  $\gtrsim 1 - 6 \times 10^{10} \text{ M}_\odot$  that corresponds to absorption path-lengths  $l > 139 \text{ kpc}$ , i.e. far beyond the central regions of the Galaxy. Our results show that the hot gas phase in galaxies like the Milky Way and Andromeda is an ideal reservoir of baryons that can comprise up to  $\sim 35\%$  of the total baryonic content of the galaxies, and up to  $\sim 75\%$  of the gas content. We also computed the amount of gas in the cold phase (within the inner 10 kpc and excluding the gaseous disc, as to be comparable with available observations), and found values of  $\sim 10^8 \text{ M}_\odot$  for both simulated galaxies, in agreement with observational results.

- We have studied the amount and distribution of the H I neutral gas phase. The majority of neutral gas around our simulated galaxies has typical column densities in the range  $N_{\text{HI}} \sim 10^{17} - 10^{18} \text{ cm}^{-2}$ , and is mainly located within a distance of about 50 – 70 kpc from their centre resembling the observed distribution of HVCs in the Milky Way and Andromeda (see Fig. 10). Higher column density clouds, i.e. those with  $N_{\text{HI}} \sim 10^{18} - 10^{20} \text{ cm}^{-2}$ , are also present within the haloes although their distribution is presumably underestimated owing to the limited resolution of our simulation. After excluding the galactic discs, the resulting mass content of *all* H I surrounding the simulated MW<sup>c</sup> and M31<sup>c</sup> is  $M(r \leq 50 \text{ kpc}) \approx 3 - 4 \times 10^8 \text{ M}_\odot$ , in line with observations. We found that this gas is typically not associated to satellite systems, but belongs to the ambient medium. Its spatial distribution tends to be more spherical than that of gas with higher column densities. If we, instead, consider H I material with higher column density values these mass estimates can decrease, at most, by a factor of a few. Typical mean velocities of accreting neutral gas with  $N_{\text{HI}} \gtrsim 10^{18} \text{ cm}^{-2}$  are of the order of  $\sim 50 \text{ km s}^{-1}$  with respect to the centre of the galaxies.

- We calculated the covering fraction of neutral gas given by our simulation in two different ways, in order to compare with different available observations. First, we projected the H I distribution of M31<sup>c</sup> as seen from the MW<sup>c</sup>, as well as the other way around. We found that the projected covering fractions  $f_c$  decline with radius; however, the steepness of the profile depends on the viewing angle. For example, the projected covering fractions, assuming  $N_{\text{HI}} > 7 \times 10^{17} \text{ cm}^{-2}$ , and at a projected distance of 30 kpc from the corresponding centre, are  $\sim 0.3$  and  $\sim 1$  for M31<sup>c</sup> and the MW<sup>c</sup>, respectively. Clearly, the projected covering fraction of M31<sup>c</sup> is much smaller than that of MW<sup>c</sup> at this distance. The reason is that, as seen from the MW<sup>c</sup>, M31<sup>c</sup> appears almost edge-on (therefore the region covered by the high column density gas looks smaller), while the MW<sup>c</sup>, as seen from M31<sup>c</sup>, appears almost face-on (and covers a



much larger projected area). We can compare the covering fractions of M31<sup>c</sup> at 30 kpc and 50 kpc with the modelling of R12. We obtain  $f_c(30 \text{ kpc}) = 0.3$  and  $f_c(50 \text{ kpc}) = 0.1$ , in line with the trend found by R12 for Andromeda. We also calculated the covering fraction of neutral gas from an all-sky H I map, as “observed” from the mock LSR of the MW: we found, for  $N_{\text{HI}} > 7 \times 10^{17} \text{ cm}^{-2}$ , a covering fraction of  $f_{c,\text{all-sky}} \approx 0.3$  (0.2) when including (excluding) the MW<sup>c</sup> neutral gas disc. These values are similar to the covering fractions obtained by Lockman et al. (2002) and Wakker (2004) by means of Milky Way H I observations.

- We calculated the accretion rates, as a function of radius, for the hot, cold and H I components of the simulated MW<sup>c</sup> and M31<sup>c</sup>. We found that, at distances close to the virial radii of the galaxies, the gas accretion rate is dominated by hot material, reaching values of  $\sim 7 - 10 M_{\odot} \text{ yr}^{-1}$ , whereas cold material has typical infall rates of  $\sim 3 - 5 M_{\odot} \text{ yr}^{-1}$ . At distances smaller than  $\sim 50 \text{ kpc}$  the situation is reversed: the accretion rate of cold gas tends to be higher than that of hot gas. This behaviour is directly related to the larger cooling efficiency of cold material in comparison with gas at higher temperatures. In general – and irrespectively of metallicity – the cooling curves of the gas peak around  $T \sim 10^5 \text{ K}$ , a temperature magnitude that is most commonly found in the inner galactic halo. As a result, the corresponding accretion rates of cold material in the central regions tend to increase.

- In our model, the MW<sup>c</sup> and M31<sup>c</sup> also accrete H I gas reaching a peak of about  $0.25 M_{\odot} \text{ yr}^{-1}$  for a distance of 20 kpc, and decrease significantly for larger distances. Interestingly, most of the H I accretion outside the discs takes place at distances of  $\sim 50 - 70 \text{ kpc}$  at a rate of about  $0.01 - 0.1 M_{\odot} \text{ yr}^{-1}$  in agreement with HVC observations. The *integrated* H I accretion rates within a sphere of 50 kpc radius (excluding the H I galactic disc) give values of  $0.34 M_{\odot} \text{ yr}^{-1}$  and  $0.22 M_{\odot} \text{ yr}^{-1}$  for MW<sup>c</sup> and M31<sup>c</sup> respectively, in line with recent observational estimates for the Milky Way. If we consider neutral material with typical HVC column densities we obtain similar results: e.g., at  $N_{\text{HI}} \geq 10^{19} \text{ cm}^{-2}$  we get  $0.28 M_{\odot} \text{ yr}^{-1}$  for MW<sup>c</sup> and  $0.16 M_{\odot} \text{ yr}^{-1}$  for M31<sup>c</sup>. In general, these accretion rate values are smaller than the SFRs of our simulated galaxies which are of the order of  $1 M_{\odot} \text{ yr}^{-1}$  (see Scannapieco et al. 2014). However, most of the cold gas accretion in the simulation is not neutral but ionized, having typical values that are larger than the corresponding galactic SFRs.

- We also calculated ejection rates for the simulated MW<sup>c</sup> and M31<sup>c</sup>. At distances close to the virial radii of the galaxies, we found that the gas ejection rate is dominated by hot material, reaching values of  $\sim 3 - 6 M_{\odot} \text{ yr}^{-1}$ , whereas the ejection of cold material is small in comparison ( $\sim 0.1 M_{\odot} \text{ yr}^{-1}$ ). This can be understood by the fact that most of the ejected material is at high temperatures as a result of the supernova feedback process. At distances smaller than  $\sim 50 \text{ kpc}$  the ejection rate of cold gas ( $\lesssim 0.1 - 1 M_{\odot} \text{ yr}^{-1}$ ) is lower than that of hot gas ( $\lesssim 3 - 4 M_{\odot} \text{ yr}^{-1}$ ), as expected. In both galaxies, the net infall (accretion minus ejection) rate profiles show a clear transition scale, located at a distance of about

100 – 120 kpc, above (below) which the hot material of the halo is being mainly accreted (ejected) as a result of the interplay between supernova feedback and gravity.

We have calculated a number of properties of the simulated LG at larger scales, say 1 – 2 Mpc, and investigated the gas distribution between the MW<sup>c</sup> and M31<sup>c</sup> systems. In this respect, we found the following main results:

- The gas associated to the simulated LG, within a distance of  $\sim 1 \text{ Mpc}$ , is dominated by the hot component, with a hot gas fraction of  $\sim 80\%$ . This means that a considerable fraction of the gas in the LG is most likely in a hot gas phase that is difficult to detect observationally. At this scale, the resulting baryon fraction is 0.13, i.e.  $\sim 20\%$  below the universal value, as could be expected from cosmic variance. Within the individual MW<sup>c</sup> and M31<sup>c</sup> haloes, the baryon fraction is even lower (0.095 and 0.087 for the MW<sup>c</sup> and M31<sup>c</sup>, respectively) suggesting that galactic winds have played an important role in ejecting baryons in the form of gas away from the haloes (see Fig. 2).

- We detected an excess of gas in the direction joining the MW<sup>c</sup> and M31<sup>c</sup> galaxies as a result of the overlapping of their hot gaseous haloes. In comparison with other random directions, this signal represents a  $\sim 20\sigma$  detection. Our gas density estimate between the two galaxies is consistent with the electron number densities derived by several authors, as it is shown in Fig. 16. In particular, at distances close to the virial radius of the MW<sup>c</sup> we found an Hydrogen number density of  $n_{\text{H}} \sim 4 \times 10^{-5} \text{ cm}^{-3}$ , which is close to the electron number density estimated by Blitz & Robishaw (2000) for path-lengths  $l \lesssim 250 \text{ kpc}$ . Interestingly, the existence of neutral gas clouds between the simulated galaxies goes in line with the observations of Wolfe et al. (2013) for the Andromeda/M33 system. We found that, in our simulation, the excess originates at  $z \sim 1$ , when the two galaxies start sharing the same filament and have overlapping gas distributions. The gas bridge we detect at  $z = 0$  may explain the relatively strong O VI absorption observed towards the direction of Andromeda (Sembach et al. 2003; Wakker et al. 2003). However, caution must be taken with this interpretation since the observed line of sights are in the same *general* direction of other prominent neutral gas structures in the Milky Way halo, such as the HVC Complexes A, C, H and the Magellanic Stream.

## ACKNOWLEDGEMENTS

S.E.N. acknowledges support from the Deutsche Forschungsgemeinschaft under the grants MU1020 16-1 and NU 332/2-1. C.S. acknowledges support from the Leibniz Gemeinschaft through grant SAW-2012-AIP-5 129. The simulation was performed on the Juropa supercomputer of the Jülich Supercomputing Centre (JSC). We thank the CLUES collaboration (www.clues-project.org) for providing the initial conditions for the constrained simulations used in this study.

## REFERENCES

- Agertz O., Moore B., Stadel J. et al., 2007, MNRAS, 380, 963
- Anders E., Grevesse N., 1989, GeCoA, 53, 197
- Anderson M. E., Bregman J. N., 2010, ApJ, 714, 320
- Asplund M., Grevesse N., Sauval A. J., Scott P., 2009, ARA&A, 47, 481
- Aumer M., White S. D. M., Naab T., Scannapieco C., 2013, MNRAS, 434, 3142
- Blitz L., Robishaw T., 2000, ApJ, 541, 675
- Braun R., Thilker D. A., 2004, A&A, 417, 421
- Braun R., Thilker D. A., Walterbos R. A. M., Corbelli E., 2009, ApJ, 695, 937
- Bregman J. N. 2007, ARA&A, 45, 221
- Bregman J. N., Lloyd-Davies E. J., 2007, ApJ, 669, 990
- Collins J. A., Shull J. M., Giroux M. L., 2005, ApJ, 623, 196
- Collins J. A., Shull J. M., Giroux M. L., 2009, ApJ, 705, 962
- Dolag K., Borgani S., Murante G., Springel V., 2009, MNRAS, 399, 497
- Fang T., Bullock J., Boylan-Kolchin M., 2013, ApJ, 762, 20
- Fernández X., Joungh M. R., Putman M. E., 2012, ApJ, 749, 181 (F12)
- Gottlöber S., Hoffman Y., Yepes G., 2010, arXiv:1005.2687
- Greveich J., Putman M. E., 2009, ApJ, 696, 385
- Gupta A., Mathur S., Krongold Y., Nicastro F., Galeazzi M., 2012, ApJL, 756, L8
- Herenz P., Richter P., Charlton J. C., Masiero J. R., 2013, A&A, 550, A87
- Hoffman Y., Ribak E., 1991, ApJL, 380, L5
- Hopkins P. F., 2013, Pressure-Entropy SPH: Pressure-entropy smooth-particle hydrodynamics
- Joungh M. R., Putman M. E., Bryan G. L., Fernández X., Peek J. E. G., 2012, ApJ, 759, 137 (J12)
- Kalberla P. M. W., Burton W. B., Hartmann D., Arnal E. M., Bajaja E., Morras R., Pöppel W. G. L., 2005, A&A, 440, 775
- Kalberla P. M. W., Haud U., 2006, A&A, 455, 481
- Kereš D., Katz N., Weinberg D. H., Davé R., 2005, MNRAS, 363, 2
- Kerp J., Winkel B., Ben Bekhti N., Flöer L., Kalberla P. M. W., 2011, Astronomische Nachrichten, 332, 637
- Klypin A., Hoffman Y., Kravtsov A. V., Gottlöber S., 2003, ApJ, 596, 19
- Lehner N., Howk J. C., 2011, Science, 334, 955
- Lehner N., Howk J. C., Thom C., Fox A. J., Tumlinson J., Tripp T. M., Meiring J. D., 2012, MNRAS, 424, 2896
- Levine E. S., Blitz L., Heiles C., 2006, ApJ, 643, 881
- Levine E. S., Heiles C., Blitz L., 2008, ApJ, 679, 1288
- Lockman F. J., Murphy E. M., Petty-Powell S., Urlick V. J., 2002, ApJS, 140, 331
- Mathur S. 2012, arXiv:1211.3137
- Miller M. J., Bregman J. N., 2013, ApJ, 770, 118
- Navarro J. F., Steinmetz M., 1997, ApJ, 478, 13
- Oosterloo T., Fraternali F., Sancisi R., 2007, AJ, 134, 1019
- Putman M. E., Peek J. E. G., Joungh M. R., 2012, ARA&A, 50, 491
- Read J. I., Hayfield T., 2012, MNRAS, 422, 3037
- Ribas I., Jordi C., Vilardell F., Fitzpatrick E. L., Hilditch R. W., Guinan E. F., 2005, ApJL, 635, L37
- Richter P. 2006, in Roeser S., ed., Reviews in Modern Astronomy Vol. 19 of Reviews in Modern Astronomy, Ludwig Biermann Award Lecture: High-Velocity Clouds and the Local Intergalactic Medium (With 12 Figures). p. 31
- Richter P. 2012, ApJ, 750, 165
- Richter P., Charlton J. C., Fangano A. P. M., Bekhti N. B., Masiero J. R., 2009, ApJ, 695, 1631
- Richter P., Paerels F. B. S., Kaastra J. S., 2008, SSRv, 134, 25
- Rosenberg J. L., Schneider S. E., 2003, ApJ, 585, 256
- Sawala T., Guo Q., Scannapieco C., Jenkins A., White S., 2011, MNRAS, 413, 659
- Sawala T., Scannapieco C., White S., 2012, MNRAS, 420, 1714
- Scannapieco C., Gadotti D. A., Jonsson P., White S. D. M., 2010, MNRAS, 407, L41
- Scannapieco C., Tissera P. B., White S. D. M., Springel V., 2005, MNRAS, 364, 552
- Scannapieco C., Tissera P. B., White S. D. M., Springel V., 2006, MNRAS, 371, 1125
- Scannapieco C., Tissera P. B., White S. D. M., Springel V., 2008, MNRAS, 389, 1137
- Scannapieco C., White S. D. M., Springel V., Tissera P. B., 2009, MNRAS, 396, 696
- Scannapieco C., White S. D. M., Springel V., Tissera P. B., 2011, MNRAS, 417, 154
- Sembach K. R., Wakker B. P., Savage B. D. et al., 2003, ApJS, 146, 165
- Shull J. M., Jones J. R., Danforth C. W., Collins J. A., 2009, ApJ, 699, 754
- Springel V., Wang J., Vogelsberger M. et al., 2008, MNRAS, 391, 1685
- Springel V., White S. D. M., Tormen G., Kauffmann G., 2001, MNRAS, 328, 726
- Stinson G. S., Brook C., Macciò A. V., Wadsley J., Quinn T. R., Couchman H. M. P., 2013, MNRAS, 428, 129
- Sutherland R. S., Dopita M. A., 1993, ApJS, 88, 253
- Thilker D. A., Braun R., Walterbos R. A. M., Corbelli E., Lockman F. J., Murphy E., Maddalena R., 2004, ApJL, 601, L39
- van der Marel R. P., Fardal M., Besla G., Beaton R. L., Sohn S. T., Anderson J., Brown T., Guhathakurta P., 2012, ApJ, 753, 8
- Wakker B. P. 2004, in van Woerden H., Wakker B. P., Schwarz U. J., de Boer K. S., eds, High Velocity Clouds Vol. 312 of Astrophysics and Space Science Library, HVC/IVC Maps and HVC Distribution Functions. p. 25
- Wakker B. P. et al., 2003, ApJS, 146, 1
- Wakker B. P., van Woerden H., 1997, ARA&A, 35, 217
- Wakker B. P., York D. G., Howk J. C. et al., 2007, ApJL, 670, L113
- Wakker B. P., York D. G., Wilhelm R., Barentine J. C., Richter P., Beers T. C., Ivezić Ž., Howk J. C., 2008, ApJ, 672, 298
- Werk J. K., Prochaska J. X., Tumlinson J. et al., 2014, arXiv:1403.0947
- White S. D. M., Rees M. J., 1978, MNRAS, 183, 341
- Winkel B., Ben Bekhti N., Darmstädt V., Flöer L., Kerp J., Richter P., 2011, A&A, 533, A105
- Wolfe S. A., Pisano D. J., Lockman F. J., McGaugh S. S., Shaya E. J., 2013, Nature, 497, 224

Yao Y., Nowak M. A., Wang Q. D., Schulz N. S., Canizares  
C. R., 2008, *ApJL*, 672, L21  
Zwaan M. A., van der Hulst J. M., Briggs F. H., Verheijen  
M. A. W., Ryan-Weber E. V., 2005, *MNRAS*, 364, 1467